Energy Conversion and Management xxx (xxxx) xxx

Contents lists available at ScienceDirect

Energy Conversion and Management

journal homepage: www.elsevier.com/locate/enconman

Research Paper

# Hybridization of Innovative Seawater Thermal Desalination Technologies up to ZLD with $sCO_2$ Concentrated Solar Power Plants

Ettore Morosini *, Igor Matteo Carraretto, Giampaolo Manzolini

*Politecnico di Milano, Dipartimento di Energia, Via Lambruschini 4, Milano 20156, Italy*

ARTICLE INFO

*Keywords:*
CSP+D
Solar Desalination
Electricity and Freshwater
Forward Osmosis
Membrane Distillation
Annual Analysis

ABSTRACT

The work proposes an insight into an innovative combination of thermal seawater desalination technologies (forward osmosis and membrane distillation) fed by sensible waste heat recovered from the cooler of a supercritical $CO_2$ cycle of a concentrating solar plant. The sensible heat at low temperature, from 50 to 75 °C, is exploited in the forward osmosis plant adopting a thermo-responsive draw agent, where 60% of available freshwater is separated from the seawater with a thermal consumption of 89 $kWh_{th}/m^3$. At temperatures up to 90 – 100 °C, the rejected heat is used in the vacuum membrane distillation plant with an innovative layout, bringing the brine close to crystallization and entailing a thermal consumption of 187 $kWh_{th}/m^3$. Finally, a crystallizer operated with the sensible low temperature heat from the cycle precipitates the salts, recovering part of them. The work presents a novel integration in series of various thermal desalination technologies to approach zero liquid discharge and includes the system hybridization with a next generation renewable concentrating solar plant, demonstrating the technological attractiveness in both technologies. With simulations of annual performances of the solar-power section, assuming a 100 $MW_{el}$ CSP plant in Sevilla, the annual freshwater production is evaluated at 3.39 $Mm^3$/year, with 32 kton/year of salts separated and 4040 equivalent operating hours. The proposed configuration leads to overall specific thermal consumption of 156 $kWh_{th}/m^3$, a level lower than conventional desalination solutions at constant output products, with water recovery ratio of 95%, thus reducing the issues related to brine management of commercial plants.

## 1. Introduction

Freshwater scarcity represents one of the most significant challenges of the 21st century, driven by various factors such as population growth, rapid industrialization, and intensifying effects of climate change. Currently, more than 3.6 billion people experience limited water availability for at least one month annually with projections indicating that the affected population will increase by 50 % within 2050 [1]. The global installed desalination capacity is undergoing exponential growth to meet this demand and is projected to nearly double by 2030 [2]. Reverse Osmosis (RO), the most widely deployed technology, relies on high hydraulic pressure to overcome the osmotic potential of seawater, a process that is inherently electricity-intensive, consuming approximately 4 $kWh_{el}/m^3$ of produced freshwater [3,4]. Furthermore, RO systems are limited in water Recovery Ratios (RR) to moderate values between 40 and 50% [5,6]. Similarly, thermally-driven technologies like Multi-Effect Distillation (MED) can demand a relatively limited Specific Thermal Energy Consumption (STEC), in the range of 70 – 90 $kWh_{th}/m^3$ [7] when a latent heat source above 70 °C is considered, but their operational effectiveness is largely capped by scaling phenomena which significantly limits the RR [8]. A critical, shared drawback of RO, MED and other commercial desalination technologies is the production of vast quantities of hypersaline brine effluents, given the RR in the range of 50% [9]. For this reason, in the last few years the interest for Zero Liquid Discharge (ZLD) plants has increased drastically to completely separate the water from the various salts commonly found in seawater, eventually recovering their economic value.

Research has advanced thermally driven membrane processes like Forward Osmosis (FO) and Membrane Distillation (MD) to push for RR beyond the ones of MED or RO. In a FO system, an osmotic pressure gradient between the two sides of the membrane is exploited (seawater side and draw side), while MD can run due to temperature difference across the membrane, driving vapor transport across it [10,11]. The key advantage of both technologies is their ability to operate using low-grade sensible heat (<100°C) from sources like industrial waste heat, geothermal energy, or solar thermal collectors [12] and recover the latent heat in the process by reducing the process energy consumption.

* Corresponding author.
*E-mail address:* ettore.morosini@polimi.it (E. Morosini).

https://doi.org/10.1016/j.enconman.2026.121696
Received 13 January 2026; Received in revised form 23 April 2026; Accepted 23 May 2026

**Nomenclature**

*Acronyms*

| | |
|---|---|
| CSP | Concentrated Solar Power |
| DNI | Direct Normal Irradiation |
| FO | Forward Osmosis |
| HX | Heat Exchanger |
| HTC | Heat Transfer Coefficient |
| HTF | Heat Transfer Fluid |
| HRU | Heat Rejection Unit |
| KPI | Key Performance Parameters |
| LCST | Lower Critical Solution Temperature |
| MD | Membrane Distillation |
| MED | Multi Effects Distillation |
| PCHE | Printed Circuit Heat Exchanger |
| PV | Photovoltaics |
| PHE | Primary Heat Exchanger |
| RR | Recovery Ratio |
| RO | Reverse Osmosis |
| $sCO_2$ | Supercritical Carbon Dioxide |
| STEC | Specific Thermal Energy Consumption |
| TES | Thermal Energy Storage |
| VMD | Vacuum Membrane Distillation |
| ZLD | Zero Liquid Discharge |

*Symbols*

| | |
|---|---|
| $A$ | Area [$m^2$] |
| $c_p$ | Specific Heat Capacity [kJ/kg/K] |
| $c$ | Concentration of draw solute [$\%_{wt}$] |
| $EE_{el}$ | Electric Energy [$MWh_{el}$] |
| $J_w$ | Permeate Flux [$kg/m^2$/hour] |
| $m$ | Mass [kg] |
| $\dot{m}$ | Mass flow rate[kg/s] |
| $\pi$ | Osmotic Pressure [bar] |
| $P$ | Pressure [bar] |
| $\Delta P$ | Pressure drop [bar] |
| $\rho$ | Density [$kg/m^3$] |
| $Q$ | Thermal Power [W] |
| $T$ | Temperature [°C] |
| $\Delta T$ | Temperature difference [°C] |
| $s$ | Specific Entropy [kJ/kg/K] |
| $V$ | Volume [$m^3$] |
| $\dot{V}$ | Volumetric flow rate [$m^3$/year] |
| $x$ | Salinity [$kg_{SALT}/kg_{TOT}$] |

A highly promising pathway to mitigate these challenges can be found in the symbiotic integration of desalination processes with Concentrated Solar Power (CSP) plants [13]: various works demonstrated the advantage of using the rejected heat from the steam cycle to drive a MED [14] and other more unconventional technologies [15,16]. Several techno-economic assessments, such as those by Olwig [17] and Askari [18], analyzed CSP+MED or CSP+RO configurations powered by steam Rankine cycles, reporting levelized costs of water in the range of 1 – 3 $/$m^3$, but consistently emphasizing that the integration compromises electric output due to the elevated condensation pressure required for steam extraction. Specifically, the loss of electric production of the steam cycle of the CSP plant is in the range of 3 $kWh_{el}$ per cubic meter of freshwater produced. [19,20,21]

Recent advancements in power block technology, particularly the development of high-efficiency supercritical $CO_2$ ($sCO_2$) cycles, have opened new frontiers for water and electricity cogeneration [22]. A unique thermodynamic characteristic of these advanced cycles is the rejection of considerable amounts of sensible heat over a gliding temperature range (typically 50 – 100 °C). These temperature levels are suitable to drive the abovementioned thermal desalination processes without penalizing the cycle electric efficiency. A few literature works are also available exploring CSP+D plants with MED and $sCO_2$ cycles [19,20,21]: configurations adopting multi-effects MED are discussed with STEC below 200 $kWh_{th}/m^3$, a much higher value than the one from latent heat sources.

In addition to the interest in conventional MED coupled to solar plants, previous works demonstrated the potentialities of FO with $sCO_2$ cycles to significant reduction in specific thermal consumption [23], from 150 $kWh_{th}/m^3$ of the MED to 90 $kWh_{th}/m^3$. Nevertheless, the hybridization of FO and CSP studied in literature systems for thermal desalination from CSP up to ZLD were not considered in literature, evidencing a significant literature gap which will be tackled in this work.

This work proposes a hybrid concept which sequentially combines FO with vacuum membrane distillation (VMD) to treat the highly concentrated brine from the FO unit, followed by a final thermal crystallization step. Accordingly, the innovative configuration proposed in this work shows a viable pathway toward achieving RR above 90% and approaching ZLD, while having a purely thermal system maintaining an overall specific thermal consumption below the values of MED plants in analogous CSP+D plants. The proposed plant benefits from the low STEC of the FO technology, if compared to MED with sensible heat in the 100-50°C range, and combines it with the high RR that is enabled with VMD, in series with the FO.

Conventional solutions such as MED are limited to 50% RR and cannot reach ZLD conditions, configurations combining MED and VMC with RO strongly penalizes the electric output of the CSP plant whereas FO alone is not considered for ZLD applications.

The primary objectives of this study are three-fold: (i) to push the boundaries of seawater recovery to over 90% and up to ZLD, thereby turning the concept of brine from a waste and problematic by-product into a valuable resource for mineral extraction; (ii) to drastically minimize auxiliary electricity consumption by designing a system that operates exclusively on low temperature sensible heat that otherwise would have been rejected in the environment; and (iii) to propose an unified and thermodynamically optimized integration of thermal desalination up to ZLD with dispatchable renewable energy technologies, such as CSP, made feasible by exploiting the favorable characteristics of $sCO_2$ power cycles. Among these, the last one represents a significant novelty of the work, as sensible heat sources from 100 to 50°C can be found in many energy and industrial applications, other than CSP, widening the interest of this study.

To validate this concept, the proposed framework is assessed through rigorous process simulations of a 100 $MW_{el}$ solar tower CSP plant, analyzed in a case study in Sevilla, Spain (identified in literature as an optimal location for desalination plants [24]), featuring detailed thermodynamic models of the solar field, power block, and advanced desalination layouts. The results presented herein demonstrate the profound potential of this integrated approach to concurrently achieve high-efficiency green electricity generation and truly sustainable freshwater production, projecting a course for the next generation of renewable energy system for the combined production of electricity and desalinated freshwater.

## 2. Technology description

### 2.1. Concentrating solar power integration with novel desalination plant

This work proposes the modeling of a 100 $MW_{el}$ CSP+D plant located in Sevilla, evaluating the electrical and freshwater production at design conditions and on annual basis, through an analysis with hourly

discretization. The CSP plant adopts a central solar tower receiver with conventional solar salts as heat transfer fluid and storage media, using a $sCO_2$ power cycle with maximum and minimum temperature of 550 °C and 50 °C, respectively.

The analysis of the overall plant is carried out by assuming that the operating conditions of the power cycle are always fixed, running at design point when thermal power is available in the heat transfer fluid (HTF) either from the thermal energy storage (TES) or from the receiver: this represents a typical operating condition which maximizes the plant electric output, since the TES decouples the solar radiation from the power cycle operations. Consequently, the thermal power discharged from the cycle to the desalination plant is at constant temperature levels, preventing off-design behavior of the desalination plant and thus stabilizing and guaranteeing its performances.

The innovative arrangement of the two thermal desalination technologies in series, specifically as bottom systems of the power cycle, shown in the schematic plant layout of Fig. 1. The first desalination section requires sensible heat at low temperatures, in the 50 – 75 °C range and is based on a FO plant with a thermo-responsive draw agent (Polycerin 55GI-2601) proposed in literature for this application [25]. The FO achieves a RR of about 60%, producing a brine with salts content of 8.3%wt., starting from conventional seawater with a salinity of 3.5% wt.

The second desalination section consists of a VMD bringing the salinity of the brine from 8.3%wt. to 20%wt. using sensible heat available at higher temperatures, from around 75 to 100 °C. The specific MD plant configuration includes a vacuum MD plant with commercially available ceramic tubular membranes [26]. The final step includes a crystallizer and concentrator, with low temperature heat in the 50 – 75 °C range from the cycle that brings the brine to the crystallization point and producing valuable minerals as by-products.

The layout of the heat rejection units is defined to meet the heat demand of the desalination units HRU (A) and HRU (B). The higher temperature HRU (75 – 100 °C) drives the VMD system, while the low temperature heat (50 – 75 °C) runs the crystallizer and FO.

The CSP+D coupling ensures that the desalination unit is adapted to the characteristics of the power cycle and its HRU, without affecting its operation and load profile along the year, conceptually substituting a conventional air-cooled HRU: as such, the temperature profile of rejected heat is defined by the power cycle, while the temperature match with the desalination section is matched by adapting its flow rates, composition and temperatures $T_B$, $T_C$, $T_D$ and $T_E$ from Fig. 1. Therefore, this work does not aim at investigating a trade-off between electrical and freshwater output, but it wants to showcase what is the maximum freshwater output achievable without affecting the electricity production.

As the work includes two innovative desalination technologies, models from literature have been adopted to strengthen the analysis. The summary in Table 1 lists the validation of the models adopted in terms of mass and heat transfer across the membranes for this specific application: detailed discussion of the numerical analysis of each subcomponent is reported in the respective section.

### 2.2. Forward osmosis plant

The forward osmosis plant is the first section of the overall desalination plant shown in Fig. 1 (specifically from point A to B on the brine side). Before entering the FO plant, the seawater is processed in a pretreatment section where problematic compounds (organic or chemical additives in seawater) are removed, whereas the FO membrane serves as a highly selective primary barrier, effectively rejecting multivalent ions, micropollutants, and any residual macromolecules present in the seawater feed. The specific layout and characteristics of the FO plant considered in this work are shown in Fig. 2 [30]: after the membrane,

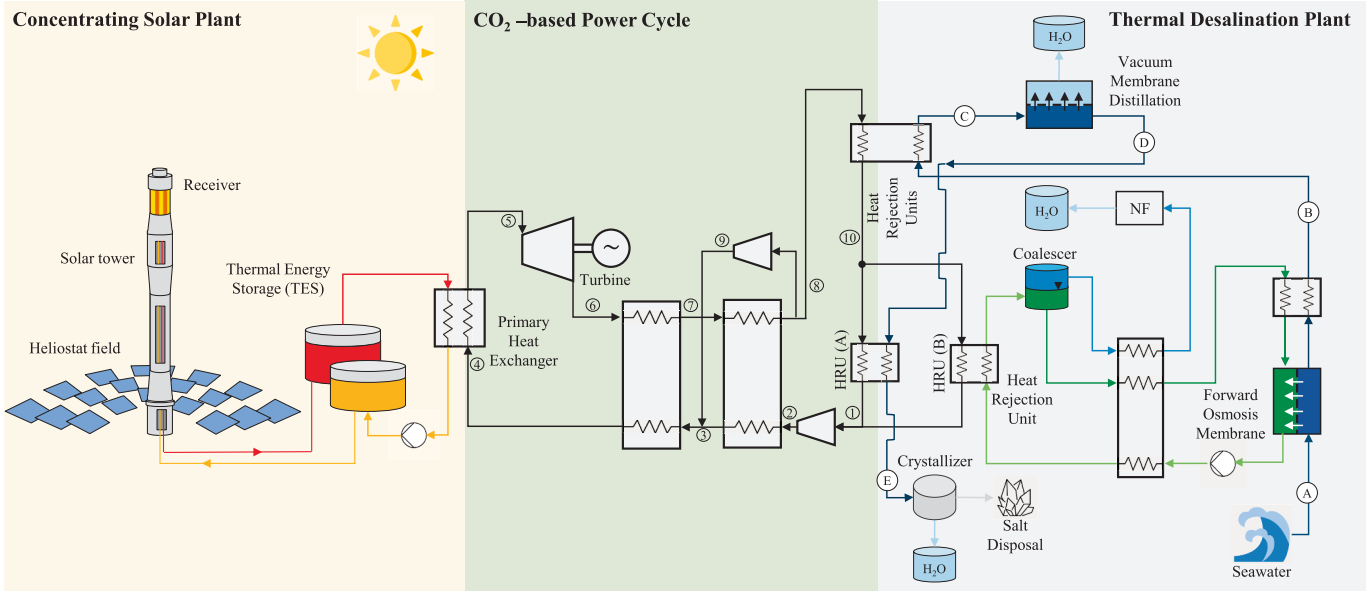


**Figure 1.** Layout of the CSP+D Plant with Waste Heat Exploitation up to ZLD.

**Table 1**
Summary of the experimental validation of the models in this work.

| Desalination Unit | Model | Deviation from Experimental Data |
|---|---|---|
| FO | $J_W$ model validated for seawater desalination | Between 5% and 13% with NaCl as draw; Always below 6% with glucose as draw [27] |
| VMD | $J_W$ model validated and membrane characteristics calibrated on this work membrane | Average deviation of 11% on $J_W$ values [28,29] |

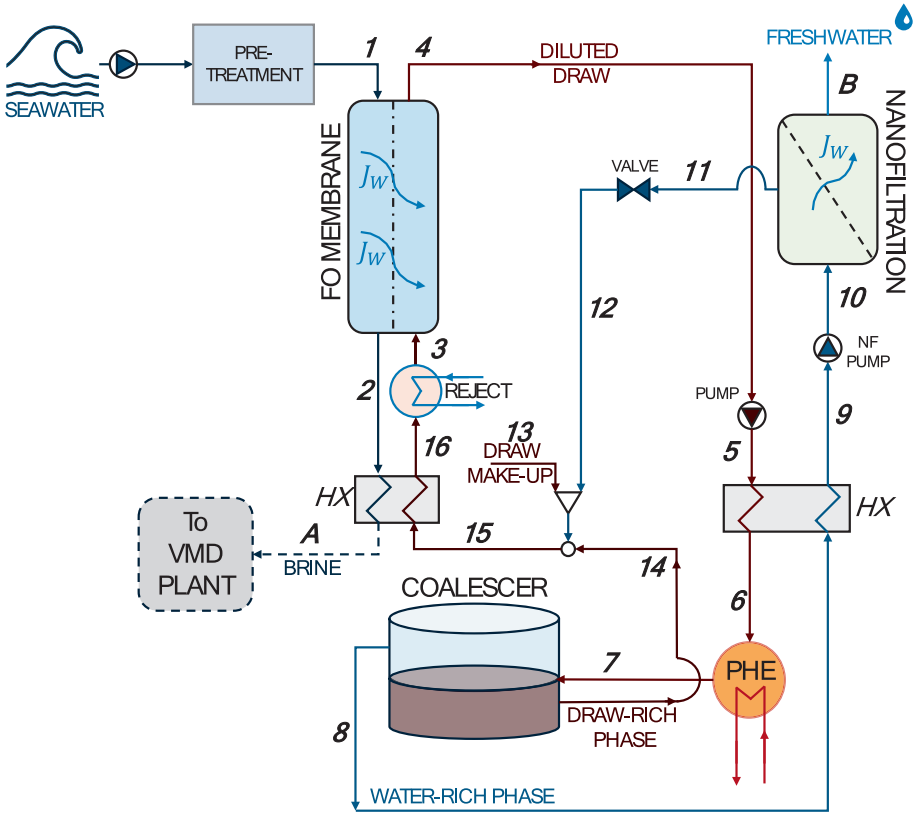


**Figure 2.** Plant layout of the forward osmosis section of the desalination plant.

the draw-rich stream (point 3) is diluted (point 4), it is heated in a recuperator up to point 6, at temperature of 45 °C, receiving heat from the cycle HRU up to point 7. After the heating phase, the mixture of both draw and water is separated into two liquid phases in a coalescer, with two compositions evaluated according to the Low Critical Solution Temperature (LCST) curve of the draw solution. Both stream are cooled down in recuperators: as the water-rich one is filtrated with a nanofiltration system producing the freshwater flow (stream B), the draw rich is directly recirculated (point 14), heating up the brine to be fed to the subsequent VMD plant.

The thermo-responsive draw agent Polycerin 55GI-2601 is considered [31] (CAS: 220144-83-2, a copolymer), guaranteeing higher RR than other polymer based draw agents as PAGB2000 as discussed in literature [32]. Properties of the mixture between Polycerin and water are summarized in Table 2.

Focusing on the Polycerin thermal properties, the heat capacity of the pure draw and the mixture between the draw and distilled water was measured at Politecnico di Milano with a calorimeter (Microcalvet Ultra, manufactured by Setaram), with the results reported in Table 3: the numerical values shown did not present relevant variations with temperature in the range 40 – 60 °C, and a polynomial interpolation of such data is derived in Table 2.

**Table 2**
Properties of Polycerin 55GI-2601 +water mixture as function of the draw mass concentration.

| Property | Correlation | Source |
|---|---|---|
| Density $\left[kg/m^3\right]$ | $\rho(c) = 141.87 \cdot c + 997.84$ | Petrinic [25] |
| Isobaric specific heat capacity $[kJ/kg/K]$ | $c_p(c) = -2.842 \cdot c^3 + 2.811 \cdot c^2 - 2.099 \cdot c + 4.180$ | This Work |
| Phase diagram (LCST) [°C] | $T(c) = 75.34 - 137.56 \cdot c + 711.57 \cdot c^2 - 1350.60 \cdot c^3 + 914.26 \cdot c^4$ | Petrinic [25] |
| Osmotic pressure $[bar]$ | $\pi(c) = 2037.60 \cdot c^{3.09}$ | Petrinic [25] |

**Table 3**
Experimental data of the Polycerin+water mixture heat capacity.

| Polycerin 55GI-2601(Mass composition) | Heat Capacity at Constant Pressure [kJ/kg/K] | Uncertainty | Operating conditions |
|---|---|---|---|
| 100% | 2.05 | 2% | From 40°C to 60°C, at ambient pressure |
| 68.4% | 3.15 | | |
| 38.2% | 3.63 | | |

Data are available on the phase diagram (i.e. the LCST of the Polycerin+water mixture) along with the osmotic pressure up to a draw concentration of 35% [25]: the equation in Table 2 reports an exponential trend of the osmotic pressure interpolated by the experimental data. Unfortunately, viscosity, thermal conductivity and diffusivity are data not available in literature for the this mixture: nevertheless, these properties do not influence the thermal consumption of the desalination plant (STEC), nor the liquid-liquid phase separation process in the coalescer and the estimation of the respective RR.

The LCST and trend of the heat capacity used in this work are visualized in Fig. 3: the draw agent requires temperatures up to 75 °C to produce pure freshwater in the water-rich stream (through the liquid-liquid phase separation in the coalescer), hence demanding quality heat, perfectly suitable for coupling with $sCO_2$ cycles.

The properties of the membrane adopted in the FO are taken from a previous literature work of the authors on FO [27], including all the geometrical and structural data, affecting only the membrane area and associated costs, whereas its water permeability is 0.44 LMH/bar [33]. The nanofiltration membrane and its characteristics is also taken from literature, characterized by a water permeability of 14 LMH/bar [34]. Once the freshwater is separated in the nanofiltration membrane (stream B in Fig. 2), the brine at the outlet of the FO membrane is heated in the recuperator up to the inlet of the VMD plant (stream A in Fig. 2): at

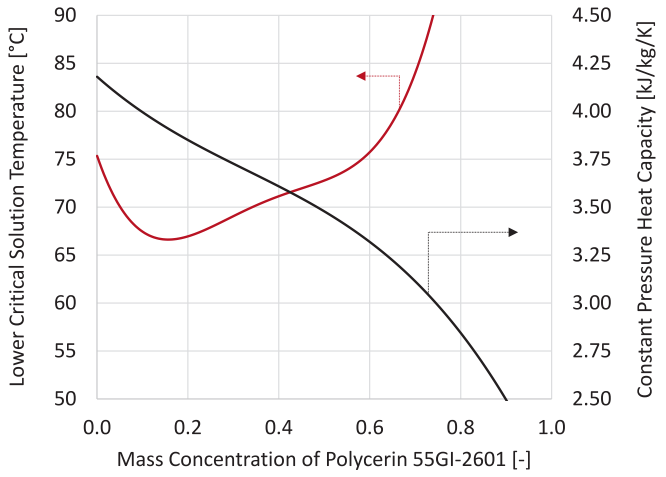


**Figure 3.** Interpolated trend of experimental data of LCST and heat capacity of the water+Polycerin 55GI-2601 mixture.

this condition the salinity is about 8.3%wt., and membrane distillation is normally considered in literature as a suitable technical solution for water permeation, avoiding problems of scaling and fouling that would affect more drastically FO or RO membranes at this high salinity levels.

Finally, the electricity consumption of the auxiliary (circulating pumps) for the water and the draw side are assessed assuming a pump efficiency of 70%, including electromechanical losses. In the calculations, the following pressure drop are assumed: i) 1 bar for the seawater, on the pre-treatment section, ii) 0.5 bar for the seawater, on the FO membrane side, iii) 1 bar for the draw side, on the coalescer, iv) 1 bar on the draw side, across the HX of the whole plant except for the nanofiltration, v) 8 bar on the draw side across the nanofiltration step. The pressure drop value across the coalescer is based on experimental data [30], whereas the value of the pressure drop across the nanofiltration step is taken from a previous work of the authors on PAGB2000 as draw solute, assuming 8 bar overpressure due to the uncertainties related to the viscosity of Polycerin 55GI-2601 and the consequent uncertainties on the corresponding NF membrane area.

### 2.3. Membrane distillation plant

The MD membranes effectively work at higher temperatures than the ones characteristic of the FO section, typically above 70 °C, as the driving force of the VMD is the pressure difference between the saturated pressure of water at the temperature of the feed and the vacuum pressure on the permeate side.

Tubular membranes are considered for VMD, available on the market from IKTS [26], with the characteristics reported in Table 4 and external diameter of 6 mm with a length of 1 m. The membrane is in $\alpha$-alumina oxide, a ceramic material, used for the good structural resistance. The brine flows in-tube as feed, while vacuum is imposed on the external side with vacuum pumps. The membrane top layer, with the highest porosity and lowest tortuosity, constitutes the internal layer, directly in contact with the feed. The intermediate layer and the support layer are coaxial

**Table 4**
Characteristics of the tubular membrane of α-AO taken from literature [29].

| | Membrane top layer | Membrane intermediate layer | Membrane support layer |
|---|---|---|---|
| Material | Alpha Alumina | Alpha Alumina | Alpha Alumina |
| Average Pore Diameter | 0.2 μm | 0.8 μm | 3 μm |
| Porosity | 43% | 42% | 36% |
| Tortuosity | 1.7 | 2.0 | 2.2 |
| Thickness | 30 μm | 15 μm | 1500 μm |

with the tubular membrane, with the support layer being in direct contact with the vacuum side. The characterization of these membranes and rigorous 1-D numerical modeling of the VMD are available in literature [29], including SEM analysis and the identification of the structural parameters such as porosity and tortuosity.

A peculiar layout of the VMD plant is developed, see Fig. 4 [29], suitable for the recovery of sensible heat from the $sCO_2$ flow in the cycle HRU, highlighted in red. According to the VMD process and layout, the heat is introduced in first two stages through two heat exchangers, red in Fig. 4, that elaborates a recirculating flow rate (flow $1_R$, flow $2_R$) higher than the main flow (flow 1).

As the vapor permeate leaves the first and second stage, it feeds in cascade the other 2 stages (third and fourth) by heating their respective recirculating flows (flow $1_P$ and $2_P$) using the latent heat to separate more water. A pinch point of 1 °C is set at the condenser of the permeate allows, useful to determine the recirculation flow of the subsequent stages (flow $3_R$, $4_R$, $5_R$, $6_R$, $7_R$, $8_R$), whereas the mixing of the recirculation stage with the main flow is set at isothermal conditions (temperature $T_{3R}$ is fixed at the value of $T_3$).

The degrees of freedom of the VMD layout are the temperature difference across the stages ($\Delta T_{STAGE} = T_1 - T_2 = T_2 - T_3 = \cdots = T_{last-1} - T_{last}$), assumed equal in all the stages and the inlet temperature of the plant ($T_1$); the salinity levels at inlet ($x_1$) depends on the previous desalination section and the outlet ($x_9$ in the figure) is set at 20%wt. with a RR for the combined FO+MD system of 85%.

The temperature difference across each stage, $\Delta T_{STAGE}$ is set to maximize the average permeate flux $J_w$ of the overall VMD plant: high $\Delta T_{STAGE}$ maximizes the permeate flux $J_w$ in the first stages but penalizes the last stages, since the condensation temperature of the last two permeate flows (flow $7_P$ and $8_P$) is kept at 40°C, while the opposite occurs with low $\Delta T_{STAGE}$. Thus, $J_w$ maximization is adopted as single selection criterion for $\Delta T_{STAGE}$ since a variation in $\Delta T_{STAGE}$ does not influence the FO section, that is precedent with respect to the brine direction, nor the subsequent crystallizer and brine separator.

The electric consumption of the vacuum pump for the VMD system is estimated, assuming a pump efficiency of 70%, including electromechanical losses. Pressure drop on the feed side is assumed at 1 bar for each stage (8 bar overall), whereas the consumption of the vacuum pump are modelled as liquid pumps of the permeate after the condensation in the respective HX, up to the ambient pressure.

### 2.4. Brine concentrator and crystallizer

Once the brine has reached a salt concentration of 20%wt., the flow is heated again up to 75 °C for the final separation step, a temperature compatible with the heat from the cycle HRU and coherent with the maximum temperature of the draw solute heated in the FO plant. The plant scheme of the brine concentrator and crystallizer is proposed in Fig. 5, adapted from literature considering the characteristics of the heat source and heat sink of this work [35], and considering the hybridization with the CSP plant with $sCO_2$ cycle.

As the brine at VMD outlet is introduced in the plant (stream “a” in Fig. 5), it is mixed with a recirculation flow from the crystallizer (stream “j”) before entering the first PHE (stream “b”) at 40°C. Then, the brine is brought to 75 °C (stream “c”) thanks to the low-temperature heat available from the HRU of the power cycle, it thus undergoes a single stage of VMD (down to stream “d” at 45°C), producing freshwater. The flow then is heated up again to the same maximum temperature of 75 °C (stream “e”) and subsequently concentrated again in a VMD stage down to 45 °C (stream “f”): finally an air-cooler brings the temperature down to 40 °C (stream “g”).

The water separated in the VMD stages (stream “i”) leads to an increase in salinity of the circulating brine above the crystallization point at 40 °C (evaluated at 26.6%wt.): for this reason, part of the salt can be separated until the salinity at the outlet (stream “h”) reaches 26.6%wt. Finally, as not all the salt introduced in the system (in stream “a”) is

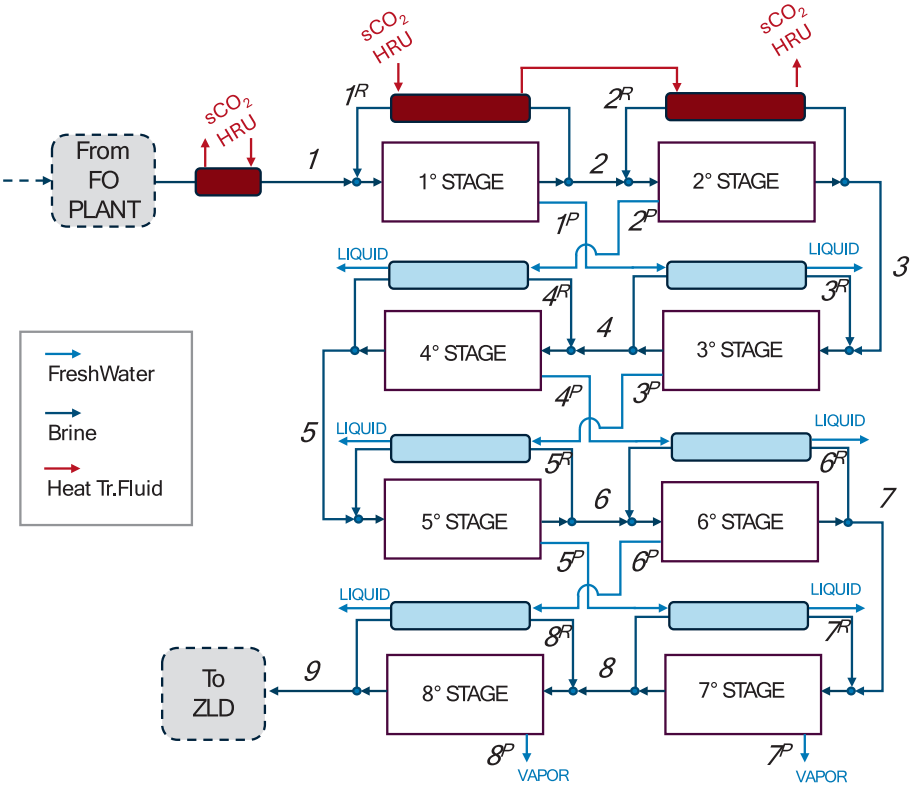


**Figure 4.** Plant layout of the vacuum membrane distillation plant, adapted from literature work of the authors [29].

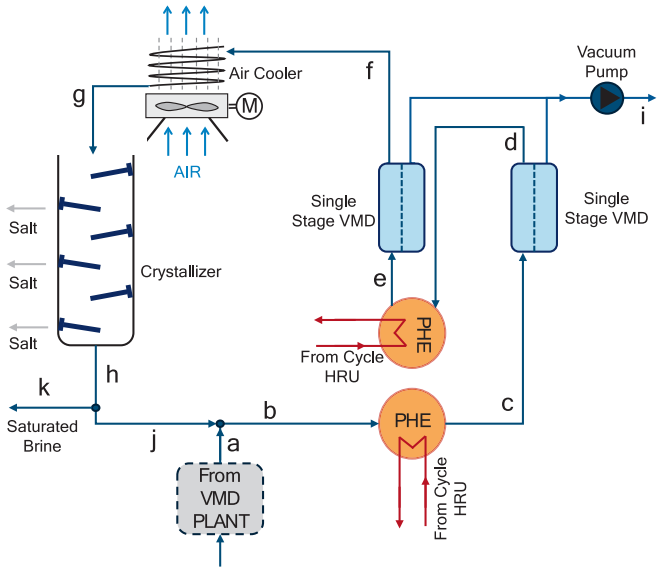


**Figure 5.** Simplified block diagram of the crystallizer.

removed in the crystallizer, an additional flow of saturated brine at 40°C is removed from the plant (stream "k"), before the flow in stream "j" can be reintroduced and mixed with the incoming brine from the VMD plant.

The process is based on the principle that the brine at the inlet of the VMD stages (at 75 °C) is far from the saturation (that occurs over 27% wt.) and water permeation remains possible, whereas at lower temperatures (40 °C) the concentration of salts necessary for the crystallization reduces, effectively separating the salt through precipitation in the crystallizer.

The process is fully integrated with the low-temperature heat available from the CSP and thus the $sCO_2$ power cycle in the 50 – 75 °C range, allowing also for the production of salt, potentially recovering its economic value.

The electrical consumption of the auxiliary is quantified as in the previous MD plant: a consumption of the vacuum pump of the condensed permeated, up to 1 bar, with an additional 5 bar of frictional pressure drop in the overall plant on the brine side including membranes, the two PHE and the air-cooler.

## 3. Modelling of the plant components

### 3.1. Solar section and power cycle for electricity production

Regarding the solar plant design and its off-design yearly analysis, along with the performance of the $sCO_2$ cycle, this work refers to a set of results taken from previous works, published in the open literature by the authors, on hybridization between a CSP plant and a seawater desalination plant based on a conventional MED system [36]. The aerial view of the solar field and the temperature-entropy diagram of the $sCO_2$ cycle are shown in Fig. 6. Moreover, the characteristics and features of the solar field and the power cycle that are most relevant for the numerical simulation and characterization of the hybrid CSP+D plant are listed in Table 5.

The solar field was designed with the open-source tool Solarpilot [37], assuming the tower and receiver height, including the heliostats dimensions, of the Crescent Dunes CSP plant in Nevada [38]. The optical performance at off-design conditions of the field, for any sun position, was also performed in Solarpilot. The thermal efficiency of the external cylindrical solar receiver was evaluated with a thermal model from Gentile [39], accounting for conductive, convective and radiating losses: simulations are run covering a wide range of thermal power on the receiver, from 20% to 100% of the nominal value to capture all possible conditions of the plant in off-design conditions, and also the modeling of the electric power absorbed by the HTF pump is characterized with the same approach.

The annual analysis of this work is carried out on hourly basis:

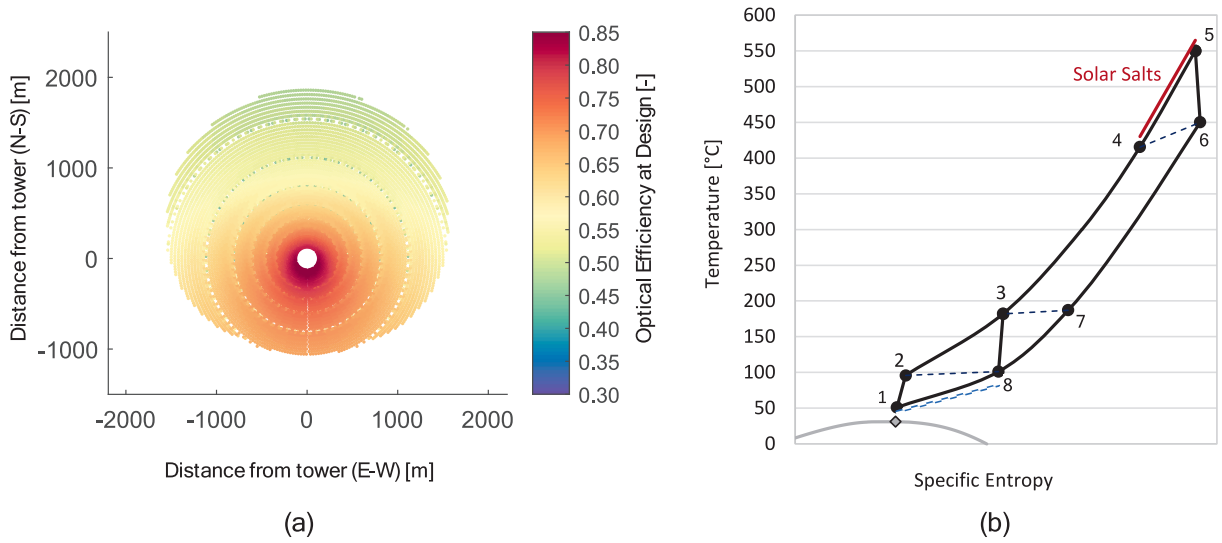


**Figure 6.** Aerial view of the CSP solar field and optical performance (a), T-s diagram of the $sCO_2$ cycle in solarized condition (b). Figures from a previous work of the authors [36].

**Table 5**
Review of the characteristics of the CSP plant and the Power cycle as from literature [36].

| Solar Field Characteristic | Value at Design | Power CycleCharacteristic | Value at Design |
|---|---|---|---|
| Location / Sun position | Sevilla, Solar Noon | Maximum Temperature [°C] | 550 |
| DNI at design [W/m$^2$] | 950 | Minimum Temperature [°C] | 51 |
| Heliostats area / Field footprint [m$^2$] | $1.28{\cdot}10^6$ / $7.07{\cdot}10^6$ | Maximum / minimum Pressure [bar] | 250 / 100 |
| HTF | Solar Salts | Turbine Isentropic Efficiency [%] | 92 |
| HTF inlet/outlet temperature [°C] | 420 / 565 | Compressors Isentropic Efficiency [%] | 88 |
| Optical / Thermal Efficiency [%] | 62.9 / 85.4 | Recuperator internal Pinch [°C] | 5 |
| Power to HTF [$MW_{th}$] | 635.4 | HRU / PHE pressure loss [bar] | 2 / 4 |
| Electric power HTF pump [$MW_{el}$] | 12.1 | Recup. pressure loss HP / LP [bar] | 0.5 / 1 |
| TES Size [h] | 8 | Net Cycle Efficiency [%] | 42.0 |

starting from the sun position and the DNI from hourly weather data of the Solarpilot database, the optical and thermal efficiencies are inferred, evaluating the energy transferred to the HTF. With a simple control algorithm, assuming the power cycle operation always at full load, the thermal energy from the HTF is evaluated for the power production and the storage in each hour of the day: to do so, a direct storage layout with eight equivalent hours is introduced, leading to a negligible amount of energy defocused along the whole year.

The power cycle simulations have been computed with the Span and Wagner equation of state [40], normally adopted for $CO_2$: the cycle maximum temperature and pressure are conventional values for cycle simulations for state-of-the-art CSP plants, along with the HX internal pinch and pressure losses [41,42]. The recompression cycle layout is chosen, suggested in the open literature for an effective coupling with the CSP plant [43]. The resulting net cycle efficiency, including electromechanical losses, is 42%. The cycle is operated always at full load, when thermal energy is available from the field or the TES it is introduced in the primary HX (PHE), and independent from the environmental conditions such as ambient temperature: this is necessary to keep the temperature profiles in the HRU of the cycle constant, hence leading to constant temperatures and heat duty in both desalination sections, FO and VDM.

### 3.2. Forward osmosis plant for freshwater production

The governing equations used to describe the FO process across the membrane are here recalled. The model for heat and mass transfer across the FO membrane is taken from the work of Colciaghi [27], where the asymmetric membrane has the active layer facing the feed solution [44]. The difference in concentration across the active layer of the membrane, which is the driving force of the whole process, is smaller than the concentration difference at the bulk of the two sides due to the concentration polarization losses included in the model. Specifically, two different concentration polarization effects have to be accounted for: (i) internal concentration polarization and (ii) external concentration polarization (the former occurs in the support layer, whereas the latter at the feed side interface).

Hence, the water flux $\left(J_w[\mathrm{kg\,m^{-2}\,h^{-1}}]\right)$ across the membrane could be described as [45]:

$$J_w = D(\pi_{Di} - \pi_{Fm}) \tag{1}$$

Where $D[\mathrm{kgm^{-2}h^{-1}bar^{-1}}]$ is the water permeability and $\pi[\mathrm{bar}]$ is the osmotic pressure. In addition, part of the draw solute can cross the membrane, increasing the concentration of the feed side. This flux of draw solute is called reverse draw solute flux $\left(J_s[\mathrm{kg\,m^{-2}\,h^{-1}}]\right)$, which is linearly proportional to the concentrations difference across the active layer:

$$J_s = B(C_{Di} - C_{Fm}) \tag{2}$$

Where $B[\mathrm{kgm^{-2}h^{-1}}]$ is the draw solute permeation coefficient, and $C$ $[\mathrm{kg\,m^{-3}}]$ is the concentration of the solute. This loss in draw solute ($J_s$) is integrated into the layout as a pure stream (referring to stream 13 of Fig. 2), but it is almost negligible from a numerical point of view with respect to the water permeated ($J_W$) and for this reason is neglected in the next step of the analysis.

The numerical model is developed across the membrane length with

a 1-D approach, discretizing the domain in 100 finite-elements of constant area: the feed and permeate properties (temperature, composition, flow rate, osmotic pressure) are evaluated locally, obtaining an accurate solution of the problem.

Once the water flux ($J_w$) is evaluated, the water permeated across the membrane $\dot{m}_w[\mathrm{kg\,s^{-1}}]$ is computed, being $\rho_w[kgm^{-3}]$ the water density and $A_{membr}[\mathrm{m^2}]$ the active area of the membrane :

$$\dot{m}_w = J_w \rho_w A_{membr} \tag{3}$$

Finally, since the osmotic pressure of the seawater depends both on temperature and salinity, the mass transfer and heat transfer model across the membrane are solved simultaneously. To do so, the heat transfer across the membrane $q''\left[\mathrm{W\,m^{-2}}\right]$ is evaluated according to:

$$q'' = UA_{membr}\Delta T_{ml} \tag{4}$$

With $U\left[\mathrm{W\,m^{-2}\,K^{-1}}\right]$ being the overall heat transfer coefficient and $\Delta T_{ml}[\mathrm{K}]$ the mean logarithmic temperature difference, where $U$ is computed as follows:

$$U = \frac{1}{\frac{1}{h_f} + R_m + \frac{1}{h_d}} \tag{5}$$

And $h_f$ and $h_d$ $\left[\mathrm{W\,m^{-2}\,K^{-1}}\right]$ are the convective heat transfer coefficients on the feed and draw side, respectively, evaluated according to conventional correlations for flat plates, and $R_m$ $\left[\mathrm{m^2K^{-1}}W^{-1}\right]$ is the conductive resistance across the membrane [27].

### 3.3. Vacuum membrane distillation plant for freshwater production

The governing equations used to describe the MD process across a porous membrane are here recalled: they are taken from the heat and mass transfer model for VMD already developed in literature by the authors [29]. These equations are derived from the works of Zhang [46] and of Kast and Hohenthanner [11], which have been widely used by other authors [10]. As for the FO model, also the VMD model is developed with a discretized 1-D approach, where the trend of the flow properties and the permeate flux are evaluated along the axial coordinate of the tubular membranes.

The mass transfer mechanism of freshwater across the membrane pores is driven by both Knudsen diffusion and Poiseuille flow (i.e., viscous flow). Hence, the permeate water flux $N\left[\mathrm{kmol\,m^{-2}}s^{-1}\right]$ is equal to the sum of these two components:

$$N = N_K + N_P \tag{6}$$

Where

$$N_K = \frac{8}{3}\frac{\epsilon r}{\tau t}\sqrt{\frac{1}{2\pi R M_m T_{wall}^{feed}}}\Delta P_* \tag{7}$$

And

$$N_P = \frac{1}{8\mu}\frac{\epsilon r^2}{\tau t}\frac{P_m}{R T_{wall}^{feed}}\Delta P_* \tag{8}$$

Specifically, $T_{wall}^{feed}$ [K] is the feed temperature at the surface of the membrane, $M_m[\mathrm{kgkmol^{-1}}]$ is the water molar mass, $R$ $\left[\mathrm{m^2kg\,s^2kmol^{-1}K^{-1}}\right]$ is the universal gas constant, $\mu[\mathrm{Pa\,s}]$ is the viscosity of the vapor across the pores, $P_m[\mathrm{Pa}]$ is the mean pressure in the pores, defined as the mathematical average between the pressure on the permeate side (i.e., the vacuum pressure, $P_{vacuum}^{permeate}$[Pa]) and the vapor pressure of water at the wall temperature of the feed side ($P_{sat}(@T_{wall}^{feed})$[Pa]). Moreover, $r$[m] is the average pore radius of the membrane, $\epsilon[-]$ is the membrane porosity, $\tau[-]$ is the tortuosity of the membrane pores and $t$[m] is the membrane thickness.

The pressure difference ($\Delta P_*$[Pa]), which is the driving force of the VMD process, is given by:

$$\Delta P_* = P_{sat}\left(@T_{wall}^{feed}\right)x_{H_2O}\gamma_{H_2O} - P_{vacuum}^{permeate} \tag{9}$$

being the difference between the saturation pressure of pure water at the wall temperature of the feed ($P_{sat}(@T_{wall}^{feed})$), multiplied by both the molar fraction of water in the feed ($x_{H_2O}[\mathrm{kmol_{H_2O}\,kmol_{feed}^{-1}}]$) and its activity coefficient ($\gamma_{H_2O}[-]$), and the vacuum pressure on the permeate side ($P_{vacuum}^{permeate}$) imposed by the vacuum pump.

Moreover, to properly simulate the mass transfer problem across the membrane, the wall temperature on the feed side ($T_{wall}^{feed}$) has to be determined. The value is retrieved from the energy balance across the membrane according to:

$$q'' = h_f\left(T_{bulk}^{feed} - T_{wall}^{feed}\right) = J_w\Delta h_{eva} \tag{10}$$

Where $q''\left[\mathrm{W\,m^{-2}}\right]$ is the thermal power per unit of membrane area required by the VMD process, $h_f\left[\mathrm{W\,m^{-2}\,K^{-1}}\right]$ is the convective heat transfer coefficient between the feed and the membrane wall, $T_{bulk}^{feed}[\mathrm{K}]$ is the bulk temperature of the feed, $J_W[\mathrm{Kg\,m^{-2}\,s^{-1}}]$ the water flux that permeates across the membrane (being $NM_m$) and $\Delta h_{eva}[\mathrm{Jkg^{-1}}]$ is the enthalpy of evaporation of water at the feed wall temperature, $T_{wall}^{feed}$.

The first two stages are directly fed by the cooled $sCO_2$ from the HRU of the cycle, while the other stages are heated by the condensing permeate of the previous ones, with $Q_i^{in}[W]$ the thermal power feeding the stage $i^{th}$, $m_{permeated,i-2}[kgs^{-1}]$ the permeate vapor of the stage $i$-$2^{th}$, the heat capacity $C_{p,i}$ $[Jkg^{-1}K^{-1}]$ of the feed as function of temperature and salinity, while $(T_i - T_{i+1})$ is $\Delta T_{STAGE}$, already defined in Section 2.3. The thermal input $Q_i^{in}$ to the $i^{th}$ stage is shown in Eq (11):

$$Q_i^{in} = m_{permeated,i-2}\Delta h_{eva} = m_{R,i}C_{p,i}(T_i - T_{i+1}) \tag{11}$$

Evaluating $Q_i^{in}$ from the stage $i^{th}$, it is possible to determine the recirculating flow rate of the $i^{th}$ stage, $m_{R,i}[kgs^{-1}]$, thus defining the mass balance across each stage.

### 3.4. Brine concentrator and crystallizer for near ZLD processes

The brine concentrator and crystallizer shown in Fig. 5 is composed of a series of components (single stage VMD membranes, HX and crystallizer). The boundary conditions on the heat sink and heat source of this plant section are: i) hot source from the $sCO_2$ cooling as sensible heat from around 80 °C to 51 °C (see HRU A in Fig. 1), ii) ambient air at design condition of 35 °C. In the HX is assumed a pinch-point of 5 °C between the $sCO_2$ in the HRU and the circulating brine (PHE), and between the ambient air and the brine (air cooler).

The mass flow rate of recirculating brine (stream "b" in Fig. 5) is computed by considering the heat available from the cycle HRU, dividing it equally in both PHE in series, and the temperature difference across the PHE (from 40 °C to 75 °C). The two VMD single stages are proposed, similarly to the VMD of the CSP+D plant from Fig. 4, with a minimum brine temperature of 45 °C at VMD outlet to allow the condensation of the permeate at the vacuum pressure corresponding to the saturation pressure of water at 40 °C: the vapor is subsequently condensed by ambient air available at 35 °C to achieve liquid freshwater. As the single stage VMD membranes cannot recover heat internally nor in cascade, since the permeate condenses directly in contact with ambient air at the lowest possible temperature, the STEC of this section coincides with the evaporation enthalpy of water (around 650-660 $\mathrm{kWh_{th}/m^3}$), where the thermal input is taken directly from the fraction of the HRU power that is not exploited by the FO and VMD

plant.

The brine concentrator and crystallization unit, which is based a VMD membrane, is modelled with a 1-D approach according to the one from section 3.3, assuming the same membrane properties and numerical models. According to literature, the specific membrane material for VMD can work for in continuous operation for hundreds of hours maintaining a constant flux [28], being also experimentally evaluated for highly saline feed up to a mass fraction of 35% [47]. To ensure the mass balance across the whole component, the saturation conditions for the hyper concentrated brine is estimated through correlations from experimental data of aqueous solutions of NaCl depending on temperature, as the one proposed by Sparrow [48]. A pretreatment section for multivalent ions chemical precipitation is to be included before the crystallization section, already done in commercial plant, adding chemical reactants for the precipitation of $Ca^{2+}$, $Mg^{2+}$ and $SO_4^{2-}$. This step doesn't influence the thermal and electric consumption of the plant, affecting only the operative costs, and thus is not detailed in this work.

Precipitated salt is removed under the form of a slurry, sold on the market to recover its economic value, whereas the saturated brine at the outlet of the brine concentrator plant is left evaporating in a dedicated small solar pond nearby the CSP plant, without recovering the water in it.

### 3.5. Key performance parameters of the CSP+D plant

A CSP+D plant is expected to produce both electricity and freshwater: as such, it can be characterized by the KPI typically adopted within the CSP community (such as optical efficiency, thermal efficiency and other ones from Table 5) and the KPI adopted in the field of thermal desalination technologies.

Moreover, it becomes important to define KPIs that can relate the thermal energy exploited from the solar section with the operation of the desalination plants. These are discussed in this section, starting from the STEC of the FO and VMD plant, including the STEC of the overall CSP+D system, and the respective RR.

According to the technology description of Section 2, the STEC $\left[\mathrm{kWh_{th}\,m^{-3}}\right]$ are proposed as:

$$STEC_{FO} = \frac{Q_{IN,FO}}{m_{Fresh,FO}} = \frac{m_6 \cdot c_{P,6} \cdot (T_7 - T_6) \cdot \rho_{H2O}}{m_B \cdot 3600} \tag{12}$$

$$STEC_{VMD} = \frac{Q_{IN,VMD}}{m_{Fresh,VMD}} = \frac{(m_{1R} \cdot c_{P,1R} + m_{2R} \cdot c_{P,2R}) \cdot \Delta T_{STAGE} \cdot \rho_{H2O}}{(\sum m_{iP}) \cdot 3600} \tag{13}$$

$$STEC_{OVERALL} = \frac{Q_{HRUsCO2}}{m_{Fresh,Overall}} = \frac{m_{sCO2Cycle} \cdot (h_8 - h_1)}{(m_{Fresh,FO} + m_{Fresh,VMD} + m_{Fresh,CRYST}) \cdot 3600} = \frac{STEC_{FO} \cdot m_{Fresh,FO} + STEC_{VMD} \cdot m_{Fresh,VMD} + STEC_{CRYST} \cdot m_{Fresh,CRYST}}{(m_{Fresh,FO} + m_{Fresh,VMD} + m_{Fresh,CRYST})} \tag{14}$$

Hence the STEC of the FO plant is evaluated considering the thermal input from the PHE (stream "6" and "7" in Fig. 2) and the freshwater produced (stream "B" of the same figure), while the STEC of the VMD plant is computed considering as thermal input the power from the $sCO_2$ HRU (red stream in Fig. 4) and output the flow rate of permeate ($1_P$, $2_P$, $3_P$, etc., from the same figure). Finally the STEC of the overall plant depends on all the freshwater produced and separated in the three subsections (including $m_{Fresh,CRYST}$, being stream "i" in Fig. 5) and the overall thermal input from the cycle HRU, $Q_{HRUsCO2}$ (from stream "8" to "1" in Fig. 1).

The RR of the FO plant is the ratio between the freshwater produced in the FO ($m_{Fresh,separated,FO}$, being $m_B$ in Fig. 2) and the fraction of freshwater within the seawater at inlet ($m_{Fresh,inlet,FO}$). In general, for any section of the desalination plant (FO, VMD and crystallizer), the RR is evaluated considering the freshwater separated in that section ($m_{Fresh,separated,i}$) and the share of freshwater at the inlet ($m_{Fresh,inlet,i}$) according to Eq (15). An analogous definition is proposed for the FO+VMD section and for the overall plant as defined below:

$$RR_{Section,i} = \frac{m_{Fresh,separated,i}}{m_{Fresh,inlet,i}} \tag{15}$$

$$RR_{FO+VMD} = \frac{m_{Fresh,Separated,FO+VMD}}{m_{Fresh,Seawater}} = \frac{m_{Fresh,Separated,FO} + m_{Fresh,Separated,VMD}}{m_{Seawater} \cdot (1 - x_{Salt,Seawater})} \tag{16}$$

$$RR_{OVERALL} = \frac{m_{Fresh,Overall}}{m_{Fresh,Seawater}} = \frac{m_{Fresh,Separated,FO} + m_{Fresh,Separated,VMD} + m_{Fresh,Separated,CRYST}}{m_{Seawater} \cdot (1 - x_{Salt,Seawater})} \tag{17}$$

Effective KPIs of hybrid plants can sometimes include details on the plant dimensions or cost. Regarding the plant dimension, indicators of HX and membrane area are relevant if compared to the overall production of freshwater along the plant operation.

In this work an indicator of the HX area included in the FO and VMD plants is evaluated with Eq. (18), being $HXArea^{Desal}_{Yearly}[m^2_{HX} m^{-3} year^{-1}]$: to do so, separated area values are presented for air-cooled HX (i.e. at membrane inlet on the draw side in Fig. 2 and for the condensation of the permeate of the 7th and 8th stage of the VMD), and for HX that only include liquid or vapor streams. For air-cooled HX, the area is evaluated assuming an ambient temperature of 35 °C, typical for hot location of CSP plants, with an overall heat transfer coefficient of 35 $W/m^2/K$ (referring to the external area of the finned surface), while a value of 1000 $W/m^2/K$ is considered for the HX with liquid or vapor streams, without finned surfaces.

Similarly to heat transfer surfaces, an indicator of the membrane area necessary for the FO and VMD plant is introduced as $MembrArea^{Desal}_{Yearly}[m^2_{membrane} m^{-3} year^{-1}]$ and evaluated as in Eq. (19): in this case, the membrane area is evaluated directly accounting for the thermal power of each separate desalination plants, the relative STEC and $J_w$.

Both KPIs present at the denominator the overall amount of freshwater produced yearly, making the indicator specific to the actual useful product of the hybrid plant.

$$HXArea^{Desal}_{Yearly} = \frac{A^{FO}_{HX} + A^{VDM}_{HX}}{m_{Fresh,Produced}} \tag{18}$$

$$MembrArea^{Desal}_{Yearly} = \frac{A^{FO}_{Membr} + A^{VDM}_{Membr}}{m_{Fresh,Produced}} \tag{19}$$

The specific freshwater production is expressed for the plant with the two KPI of Eqs. (20) and (21): the first one accounts for the instantaneous freshwater production at design conditions, being $\dot{V}^{Desal}_{Design}\left[liter\, m^{-2}_{Helio}\, hour^{-1}\right]$, while the second is an indicator of the yearly freshwater production, $V^{Desal}_{Yearly}\left[m^3\, m^{-2}_{Helio} year^{-1}\right]$. To include the plant size in the KPI, the indicators are specific to the unit of reflective area of the CSP plant (the heliostats area, $A_{Heliostat}$).

$$\dot{V}^{Desal}_{Design} = \frac{\dot{m}_{Fresh,Design}}{A_{Heliostat}} \tag{20}$$

$$V^{Desal}_{Yearly} = \frac{m_{Fresh,Yearly}}{A_{Heliostat}} \tag{21}$$

## 4. Case study: 100 $MW_{el}$ CSP+D plant in Sevilla

The results of this work outline the hybrid production of electricity and freshwater of the CSP+D plant introduced in this work and schematized in Fig. 1. As mentioned, the optical efficiency of the field, the thermal efficiency of the receiver, the TES profile and the electrical production of the solar section are evaluated with hourly discretization assuming solar resources data of the location (Sevilla).

Considering the net electric power of the $sCO_2$ cycle (100 $MW_{el}$) and the auxiliary electric consumption (mainly the power of the HTF pump, evaluated on hourly basis), the net electrical energy produced and sold to the grid is evaluated at 404 $GWh_{el}$/year, leading to a capacity factor of the solar plant of 46% and around 4040 equivalent hours per year.

The power cycle, always run at full load whenever thermal power is available either from the solar receiver or the TES, rejects to the bottom desalination section through its HRU a yearly thermal energy of 576 $GWh_{th}$/year, being the totality of the rejected heat from the cycle.

The next subsections present the resulting characteristics of the FO, VMD and crystallizer and brine concentrator plants, discussing details on the characteristics of each subsystem along with the overall KPI of the CSP+D plant as previously defined.

### 4.1. Performance of the forward osmosis plant in CSP+D configuration

According to the CSP+D scheme of Fig. 1, the first section of the desalination plant is the FO, receiving water from the sea at its natural salinity assumed at 3.5%wt. To understand and identify the most effective operating conditions of the FO layout, a wide sensitivity analysis has been carried out on the main parameters, mainly varying the ratio between the flow rate of the membrane feed (seawater) and permeate (mixture between freshwater and draw) for unit of membrane area, keeping the temperature of the draw at 40 °C, the seawater at 25 °C and the temperatures across the PHE (from stream 6 to 7 in Fig. 2) at 45 °C and 75 °C, respectively.

The temperature difference across the PHE of the FO plant is defined as follows: at first, the draw-side minimum temperature of 45 °C is set to ensure a reasonable internal pinch-point in the T-Q diagram of the power cycle HRU with a $sCO_2$ minimum temperature of 51 °C, as reported in section 3.1. Then the maximum temperature of 75 °C is chosen to allow for an effective seawater separation in the coalescer (referring to the LCST of the draw of Fig. 3). The draw concentration at membrane inlet has been fixed at 45% (stream 3), ensuring a good osmotic pressure in the permeate side, sufficient to target the $RR_{FO}$ value of 60% with seawater on the feed side.

The results in Table 6 highlight the characteristics of the streams in the FO plant under the conditions investigated, referring to the specific nomenclature reported in Fig. 2: in the table, the mass concentration refers to mass concentration of NaCl in water for streams 1, 2, A and B, and to the concentration of the draw solute in all the other ones. The resulting $STEC_{FO}$ is 89 $kWh_{th}/m^3$, considering the thermal input (from stream 6 to 7) and the permeate water with a $RR_{FO}$ equal to 60.0% favored by the draw osmotic pressure. Finally, the average permeated water flux $J_w$ is 1.18 $kg/m^2/h$, going from around 0.6 (cold side) $kg/m^2/h$ to 1.9 (hot side) $kg/m^2/h$. The nanofiltration section thanks to the infinite selectivity to the draw agent (due to the large molecular dimension of Polycerin with respect to water) can operate with small pressure difference between the two sides of the membrane with consequent negligible electric consumption of this step (differently from a conventional RO membrane for seawater desalination).

The temperature-composition chart of the FO plant is also shown, in Fig. 7, along with the FO plant layout, visualizing the heating and cooling of the draw mixture, along with the permeation of freshwater across the membrane (from 3 to 4) and the phase separation in the coalescer (from 7 to 8 and 14). It is noted that at the chosen value of the maximum temperature ($T_7$) the water-rich stream (stream 8, 9 and 10) presents only traces of draw solute, easing the operation of the nanofiltration process.

### 4.2. Performance of the VMD plant and crystallizer in CSP+D configuration

The brine at the outlet of the FO plant with a salinity of 8.3% feeds the VMD plant. Considering an inlet temperature of the feed of 83 °C, the optimal $\Delta T_{STAGE}$ is equal to 4°C (see Fig. 4) leading to an outlet brine temperature of 51 °C, well above the condensation temperature of 40 °C of flows $7_P$ and $8_P$ in the plant layout. The heat is thus introduced in the first two stages between 83 °C and 75 °C (feed side) and the main resulting variables across all the stages of the plant along the axial coordinates in Fig. 8.

The recirculation rate in the first two stages is 8.2, whereas the $STEC_{VMD}$ is 189 $kWh_{th}/m^3$. Considering the tubular membrane characteristics of IKTS, the VMD results per each stage (summarized in Table 7) depict promising values of permeate flux $J_w$, that decreases along the stages (due to the exponential trend of the water vapor pressure) and it is enhanced again in the last two stages. In these last two the driving force is enhanced with respect to the previous one, since: the vacuum pressure on the permeate side corresponds to the saturation pressure of water at 40°C, a condition enabled by the air cooling necessary for condensation of the permeate streams.

The average overall $J_w$ of 9.1 $kg/m^2/h$, an order of magnitude higher than the one of the FO sections, denotes the good features of the ceramic membranes for this application in VMD.

Finally, as the high salinity brine is rejected from the VMD plant (stream 9 in Fig. 4), it is fed to the crystallizer and brine concentrator of Fig. 5. The numerical results of Table 8 summarizes the temperatures and salinity of the streams in the plant, including the flow rate assuming as a unitary value (100% of the flow) the inlet brine from the top VMD plant (stream "a" in Fig. 5). Considering the heat available from the $sCO_2$ cycle HRU for the crystallizer, 6% of the mass flow rate of the highly concentrated stream at inlet is separated as salt, while 42% of the inlet brine at inlet is separated as pure water in the two VMD single stages (stream and "i" in Table 8). The remaining 52% of the inlet brine is rejected as saturated conditions at 40°C (salinity of 26.61%$_{wt}$) and left evaporating to achieve a complete ZLD process without recovering its water content: this saturated flow represents only 7.4% of the overall mass flow rate of the seawater at the inlet of the CSP+D plant.

The T-Q diagram of the heat supplied from power cycle HRU to the desalination plants is represented in Fig. 9: the VMD plant is run with heat from 105 °C to 80 °C, matching the hot source (cooling of $sCO_2$) avoiding internal pinch-conditions on the higher-temperature section of the HRU. Regarding the lower-temperature region, at $sCO_2$ temperatures below 80 °C, a part of the flow is used in the FO plant (HRU (B) in

**Table 6**
Conditions of the FO plant of Fig. 2.

| Point | Temperature [°C] | Flow Rate [%sea] | Concentration [%wt.] | Point | Temperature [°C] | Flow Rate [%sea] | Concentration [%wt.] |
|---|---|---|---|---|---|---|---|
| 1 | 25 | 100 | 3.50 $_{salt}$ | 10 | 46.5 | 80.0 | <1 $_{draw}$ |
| 2 | 40 | 42.1 | 8.30 $_{salt}$ | 11 | 46.5 | 22.1 | <1 $_{draw}$ |
| 3 | 40 | 97.6 | 45.0 $_{draw}$ | 12 | 46.5 | 22.1 | <1 $_{draw}$ |
| 4 | 29.6 | 155.5 | 28.3 $_{draw}$ | 13 | 25 | <0.1 | 100 $_{draw}$ |
| 5 | 29.6 | 155.5 | 28.3 $_{draw}$ | 14 | 75 | 75.5 | 58.2 $_{draw}$ |
| 6 | 45 | 155.5 | 28.3 $_{draw}$ | 15 | 67.5 | 97.6 | 45 $_{draw}$ |
| 7 | 75 | 155.5 | 28.3 $_{draw}$ | 16 | 55.7 | 97.6 | 45 $_{draw}$ |
| 8 | 75 | 80.0 | <1 $_{draw}$ | A | 64.4 | 42.1 | 8.30 $_{salt}$ |
| 9 | 46.5 | 80.0 | <1 $_{draw}$ | B | 46.5 | 57.8 | 0 $_{salt}$ |

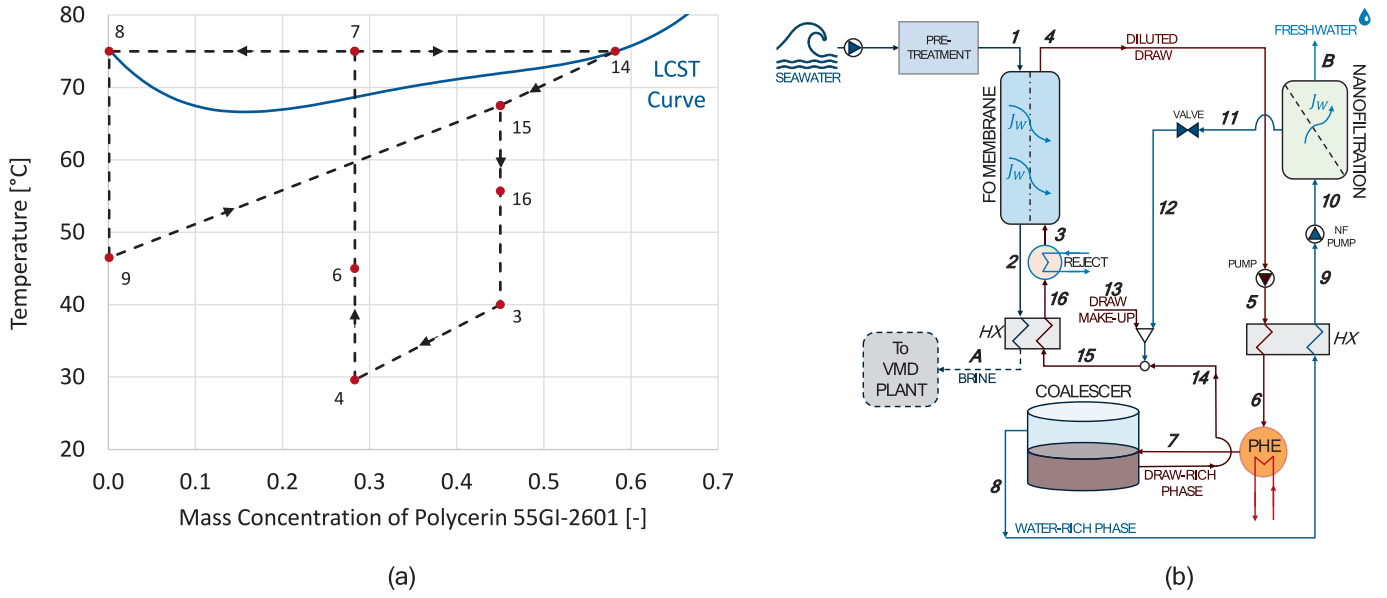


**Figure 7.** Temperature and composition behavior of the circulating flow in the FO plant with POLYCERIN 55GI-2601 as draw agent (a), FO plant (b).

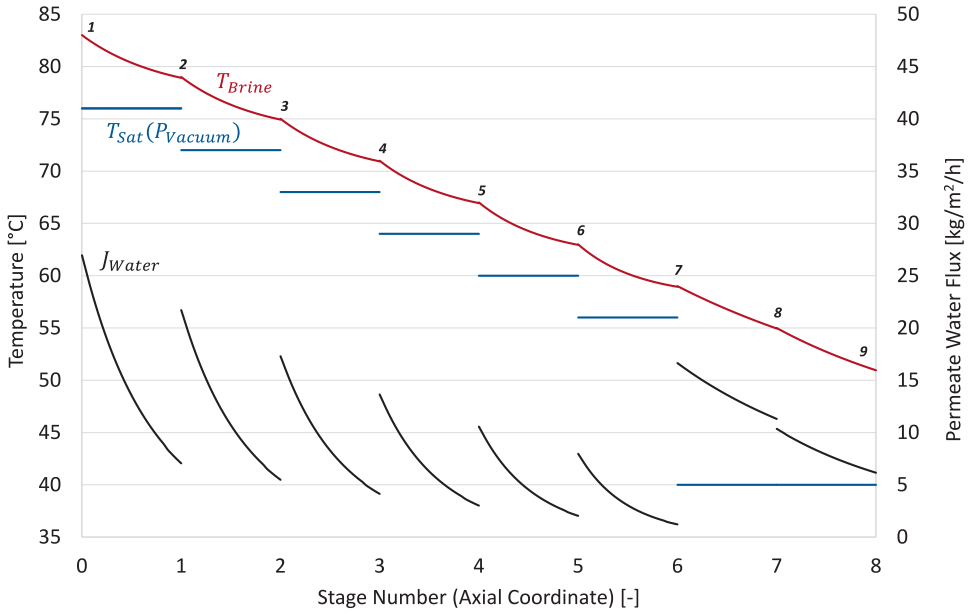


**Figure 8.** Trend of the temperature and vapor flux across the VMD plant: numbers 1 to 9 refers to the feed conditions as reported in Fig. 4.

**Table 7**
Summary of results from the VMD plant modelling.

| Stage | $J_w$ [kg/m²/h] | Outlet salinity [%wt.] | Stage | $J_w$ [kg/m²/h] | Outlet salinity [%wt.] |
|---|---|---|---|---|---|
| 1 | 14.7 | 8.90 | 5 | 5.1 | 12.75 |
| 2 | 11.7 | 9.55 | 6 | 3.6 | 14.41 |
| 3 | 9.1 | 10.40 | 7 | 13.7 | 16.78 |
| 4 | 7.0 | 11.41 | 8 | 8.0 | 20.00 |

Fig. 9 (b)) and the remaining part in the hot air crystallizer (HRU (A) in Fig. 9 (a)). With a clear understanding of the energy balance from the cycle HRU to the desalination plant, the next section investigates the overall freshwater obtained from each of the three separate plants in series, and the respective thermal performances of the separation.

### 4.3. CSP+D annual analysis and KPI: Energy and freshwater production

Considering the combined performances of the FO, MD, crystallizer and solar plant, the overall STEC ($STEC_{OVERALL}$), overall RR ($RR_{OVERALL}$) and annual energy and freshwater produced are presented. The data in Table 9 reviews the main results of each desalination technology: an overall STEC of 156 $kWh_{th}/m^3$ is obtained, with an overall freshwater RR of 95.0% and a separation of salts of 31% with respect to the salt in the seawater.

The analysis is carried out considering the water separated in the FO and VMD sections (according to the two values of RR) and their respective STEC (89 and 189 $kWh_{th}/m^3$). It results that 52.7% of the $sCO_2$ flowrate flows in HRU (B) of the FO plant, and 47.3% the $sCO_2$ flow in HRU (A). For each of the two HRU, 65% of the power is dedicated to the lower temperature heat recovery section (either FO or crystallizer), while 35% of the thermal power is exchanged in the high temperature

**Table 8**
Characterization of the circulating flows in the brine concentrator-crystallizer. streams numbers refer to the plant layout of Fig. 5.

| Point | Temperature [°C] | Flow Rate [%Inlet] | Salinity [%wt.] | Point | Temperature [°C] | Flow Rate [%Inlet] | Salinity [%wt.] |
|---|---|---|---|---|---|---|---|
| a | 40 | 100 | 20.00 | g | 40 | 478 | 27.55 |
| b | 40 | 520 | 25.34 | Salt | 40 | 6 | 100 |
| c | 75 | 520 | 25.34 | h | 40 | 472 | 26.61 |
| d | 45 | 499 | 26.40 | k | 40 | 52 | 26.61 |
| e | 75 | 499 | 26.40 | j | 40 | 420 | 26.61 |
| f | 45 | 478 | 27.55 | i | 40 | 42 | 0 |

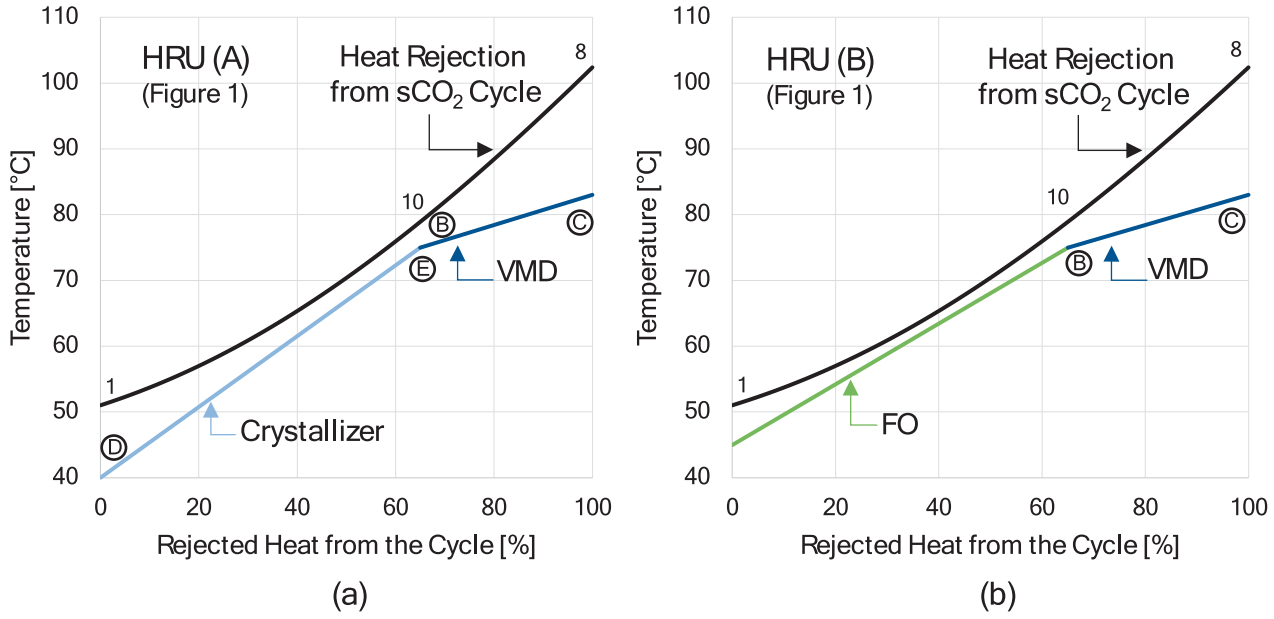


**Figure 9.** Integration between $sCO_2$ cycle heat rejection units and the three thermal desalination plants: the nomenclature in the figure refers to the one of Fig. 1.

**Table 9**
Overview of the KPI of the seawater desalination technologies applied to the CSP plant.

| | FO | VMD | Crystallizer | Overall Plant |
|---|---|---|---|---|
| STEC [$kWh_{th}/m^3$] | 89 | 189 | 660 | 156 |
| $RR_{Overall}$ [%] | 60.0 | 85.5 | 95.0 | 95.0 |
| $RR_{Section}$ [%] | 60.0 | 63.7 | 65.5 | - |
| Outlet salinity [%wt.] | 8.3 | 20 | 100 (Salts) - 26.6 (Rejected brine) | 100 (Salts) - 26.6 (Rejected brine) |
| Average $J_w$ [$kg/m^2/h$] | 1.18 | 9.1 | - | - |

section to feed the VMD plant, as shown in Fig. 9.

Considering the yearly electric energy production of 404 $GWh_{el}$/year from the solar plant, with a capacity factor of the solar plant of 46% and around 4040 equivalent hours per year, the figures in Table 10 show the annual results of the desalination and separation plant applied to the CSP plant with $sCO_2$ cycle: the yearly freshwater produced is $3.39{\cdot}10^6$ $m^3$/year, with around $32{\cdot}10^3$ ton/year of salt. Hence, starting from these results of the annual analysis, relevant KPIs of the plant are discussed in the following subsection, with focus on the necessary area for the membranes and the heat exchangers involved in the plant.

It is important to underline that previous works on CSP+D system sharing the same power plant technology provided similar annual analysis, while presenting low RR (not over 50%) hence underlining the relevance of the current study for next-generation desalination plants run by sensible heat. Specifically, referring to Doninelli's study on the MED desalination plant the STEC computed at same boundary conditions is around 130 $kWh_{th}/m^3$ [36], hence a higher freshwater production was found ($4.2 \cdot 10^6$ $m^3$/year) considering the same solar plant of this work: this comes at a cost of more problems for the brine management. Considering the work of Carraretto on the CSP+D plant located in Dubai with only single section of FO [49], the resulting STEC is evaluated at around 100 $kWh_{th}/m^3$ using PAGB2000 as draw solute: nevertheless, this low STEC value comes at a cost of a way lower RR (of around 30%, instead of this work value of 95%), that is estimated for PAGB2000

**Table 10**
Annual results of the Desalination plant.

| | FO | VMD | Crystallizer | Overall Plant |
|---|---|---|---|---|
| Power share from cycle HRU [%] | 34 | 35 | 31 | 100 |
| Thermal Power from cycle HRU [$MW_{th}$] | 47.2 | 48.2 | 42.4 | 137.8 |
| Annual Energy from cycle HRU [$GWh_{th}$/year] | 191 | 195 | 171 | 557 |
| Annual Freshwater produced [$m^3$/year] | $2.14{\cdot}10^6$ | $1.03{\cdot}10^6$ | $0.22{\cdot}10^6$ | $3.39{\cdot}10^6$ |
| Annual Salt separated [ton/year] | - | - | $32.3{\cdot}10^3$ | $32.3{\cdot}10^3$ |

as draw solute due to the poorer separation capacity to achieve water permeation across the membrane and phase separation in the coalescer, if compared to Polycerin 55GI-2601.

Considering the auxiliary consumption of the pumps mentioned in the previous desalination sections (vacuum pumps for VMD and circulation pumps), the overall electricity auxiliary consumption is very low with respect to the power plant electric production, being less than 0.5% (2.0 $GWh_{el}$/year out of the 404 $GWh_{el}$/year produced). This corresponds to a specific electric energy consumption (SEEC) of around 0.59 $kWh_{el}/m^3$ for the overall system with the RR of 95% and STEC of 156 $kWh_{th}/m^3$: the SEEC evaluated is thus between one and two order of magnitude lower than the SEEC of analogous electrical-driven MVC alternative configurations that are not fed by waste heat.

### 4.4. CSP+D annual analysis and KPI: Economic analysis and system footprint

A preliminary economic analysis is carried out, considering estimations of the capital expenditure cost (CAPEX) of the various component and evaluating the levelized cost of water (LCOW) of the CSP+D plant analyzed in this work: details on the methodology adopted for the LCOW estimation are shown in the Appendix.

The initial CAPEX of the system is estimated at 110 M€, including indirect and contingency costs, evaluated for the overall capacity of this work of 840 $m^3/h$: out of this, around half of it is related to the membranes capital costs and the second half to the capital costs of the HX. In addition to the initial CAPEX, it is assumed that all the membranes are substituted every 5 years, and their respective costs are allocated accordingly.

The resulting LCOW is 5.8 €/$m^3$ and it mainly depends on: i) the capacity factor of the solar plant which limits the capacity factor of the desalination plant to the same value, being only 46% in this work (thus different analyses of CSP with higher annual DNI would lead to lower LCOW values), ii) the membrane replacement cost, iii) the OPEX and iv) financial assumptions such as the discount rate. In detail, the LCOW is determined by the upfront capital cost for a share of 45%, the OPEX contributes for 14% of the LCOW, whereas the membrane replacement contributes for the remaining 41% of the LCOW. The analysis is carried out without any economic valorization of the separated volume of salts, considering a negligible cost of the thermal energy from cycle HRU (being effectively waste heat) and by assuming electricity consumed to be included in the OPEX.

Due to the strong sensitivity of the LCOW on the capacity factor, plant lifetime, discount rate and energy costs, a comparison with similar LCOW from literature can be difficult to be made: nevertheless, the value in this work falls within a range of 4.5 to 7 $/$m^3$ proposed in literature analyses [50].

Along with the economic analysis of the system, system footprint and component sizing are also analyzed: KPI related to HX and membrane dimension are included in Table 11. In the table, with an overall $HXArea^{Desal}_{Yearly}$ of 161 $m^2_{HX}*m^{-3}$ $10^3$*$year^{-1}$, the area of the air-cooled HX is 5 times higher than the ones with liquid or vapor streams, even if the heat transferred in the latter is much higher. Moreover, the VMD section accounts for most of the HX area, particularly for the condensation of the permeate flow at the last two stages ($7^{th}$ and $8^{th}$ stage).

Regarding the membrane area, the KPI defined as $MembrArea^{Desal}_{Yearly}$ has an overall value of 102 $m^2_{Membrane}*m^{-3}10^3*year^{-1}$, the great majority of the membrane area is disposed for the FO plant because of the lower *Jw* and the highest amount of recovered water.

A trade-off between membrane and HX area (and costs) is evidenced in the analysis: while the FO plant does not require large HX surfaces, the necessary membrane area is extremely relevant. On the other hand, due to the many subsequential condensation steps of the vapor permeate in the VMD, vast surfaces in HX are forecasted, with limited membrane area due to the inherently higher driving force of vacuum membrane distillation process.

Along with the LCOW analysis defined, a sensitivity on the main critical parameters of the desalination plant is also proposed in Fig. 10, focusing on uncertainties related to variations within reasonable range of the overall HTC of the HX (with a 25% variation with respect to the base case for both air-cooled HX and liquid-cooled ones), and the characteristics of the three categories of membrane involved. The water flux permeated of the VMD section, $J_w$, is only varied by 20%, since the a validation of the model on this membrane material is already presented in literature, whereas for both the FO and the NF a variation in water permeability of 50% is assumed, covering possible analysis for a wider range of membrane characteristics. Results suggest that variations in FO membrane water permeability don't have significant influence in LCOW, with negligible variation in LCOW for different NF water permeability, whereas the variations in HX and VMD characteristics can bring the LCOW to vary always within 5.3 to 6.3 €/$m^3$, demonstrating the robustness of the LCOW analysis.

Finally, it is important to recall that the results of this sections are relative to the annual simulations of the CSP plant in Sevilla, with a total of 4040 equivalent hours (i.e. a capacity factor of around 46%): different simulations with larger TES of the CSP plant or in locations with higher solar radiation may results in very different levels of KPIs.

With regards to the electrical section, as mentioned in section 3.1 the annual electricity production of 404 $GWh_{el}$/year by the power plant is evaluated from an overall heliostat area and footprint of $1.28{\cdot}10^6$ $m^2$ and $7.07{\cdot}10^6$ $m^2$, respectively.

Accordingly, the plant presents a specific production of freshwater $\dot{V}^{Desal}_{Design}$, at design condition (DNI of 950 W/$m^2$), of 0.302 liter/$m^2_{Helio}$/hour, whereas the same indicator on an annual basis is $\dot{V}^{Desal}_{Yearly}$, 2.65 $m^3/m^2_{Helio}$/year.

## 5. Conclusions

This work develops and exhibits a novel configuration of a hybrid CSP+D plant that is particularly effective with $sCO_2$ cycles feeding a bottom desalination plant, up to ZLD. Expanding the framework of this

**Table 11**
Details on the area of the heat exchangers and membranes involved in the FO and VMD plant.

| | HX: Liquid/Vapor | HX: Air-cooled |
|---|---|---|
| FO+NF Plant: HX Area [$m^2$] | 7 619 | 35 505 |
| VMD+Crystallizer Plant: HX Area [$m^2$] | 77 575 (VMD) + 9450 (Cryst.) | 393 469 (VMD) + 22860 (Cryst.) |
| FO+NF Plant: $HXArea^{Desal}_{Yearly}\left[\frac{m^2_{HX}}{m^3{\cdot}10^3/year}\right]$ | 2 | 10 |
| VMD+Crystallizer Plant: $HXArea^{Desal}_{Yearly}\left[\frac{m^2_{HX}}{m^3{\cdot}10^3/year}\right]$ | 26 | 123 |
| | **Membrane: FO+NF Plant** | **Membrane: VMD+Crystallizer Plant** |
| Membrane Area [$m^2$] | 307 500 (FO)+ 4700 (NF) | 28 025 (VMD) + 5855 (Cryst.) |
| $MembrArea^{Desal}_{Yearly}\left[\frac{m^2_{Membr}}{m^3{\cdot}10^3/year}\right]$ | 92 | 10 |

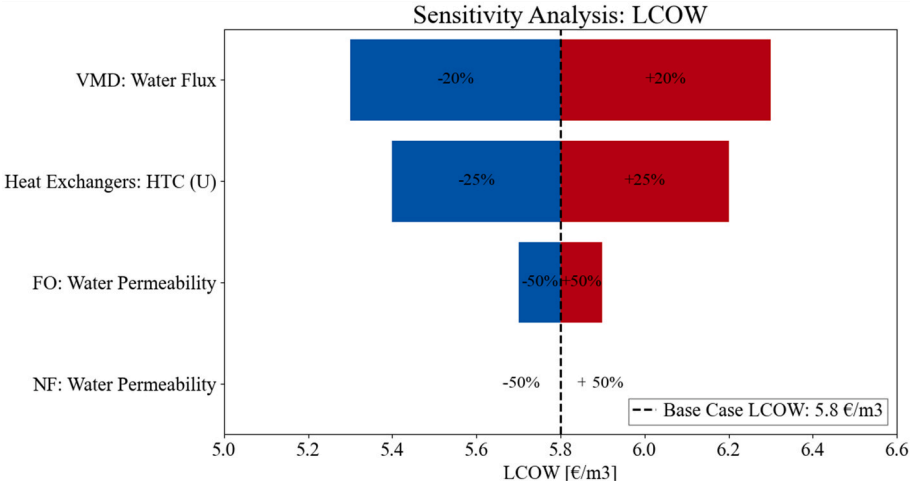


**Figure 10.** LCOW sensitivity on characteristics of HX and membranes.

study, the configuration proposed can also be extended to various applications, thanks to the accurate integration between the desalination subsections and the sensible heat source from around 100 °C to 50 °C that can be representative of any waste heat recovery process, particularly from exhaust gases at low temperature.

The performance of the systems is presented with an overall STEC of 156 $kWh_{th}/m^3$ and a recovery ratio of 95%, exploiting all the wasted and rejected heat from the power cycle, bringing the seawater to the separation between freshwater and salts.

In the first section of the work, this study demonstrates the interesting characteristics of Polycerin 55GI-2601 as draw solute in a FO plant, providing experimental data of heat capacity collected within this work: a recovery ratio of 60% can be considered feasible for this first desalination section, thanks to the promising thermophysical properties of the draw mixed with water, with a STEC of 89 $kWh_{th}/m^3$, extremely promising if compared with conventional state-of-the-art MED plants at the same heat source conditions.

Furthermore, the study evaluates the high permeate fluxes of ceramic alumina oxide tubular membrane for the VMD plant, able to desalt high salinity brines up to 20%wt. in salt without compromising the thermal consumption levels (remaining below 190 $kWh_{th}/m^3$) for a cascade plant layout.

Considering the main characteristics and the annual analysis of a 100 $MW_{el}$ CSP plant with a $sCO_2$ cycle in Sevilla, operated at full load when thermal power is available from the solar field or from the energy storage, the integration and hybridization of the proposed solar plant with the novel desalination system is particularly promising. As a matter of fact, the rejected heat from the HRU of the cycle would have been effectively wasted, impossible to be re-used for any thermal processes or direct use (such as district heating, etc.): for this reason, both the freshwater and the separated salts are effectively direct by-products of the solar plant. Results of the annual analysis of the 100 $MW_{el}$ CSP+D plant with solar tower located in Sevilla suggest that annual specific water production are possible around 2.65 $m^3_{WATER}/m^2_{HELIO}$/year, separating a large quantity of salt with a considerable market value. Moreover, the electric consumption related to the overall desalination process results almost negligible with respect to the electric energy produced by the solar plant, being less than 0.5% on annual basis, with a SEEC of 0.59 $kWh_{el}/m^3$. Finally, a preliminary economic analysis of the system suggests that the LCOW of the desalination plant is around 5.8 $€/m^3$, an interesting value for a desalination plant with a yearly capacity factor of only 46%, suggesting that this could substantially lower for CSP plants with higher capacity factors.

Future works can focus on expanding the domain of the simulations: regarding the FO plant, different draw solutions or different composition of the same draw can be considered for a more wide optimization. On the MD section, different technical solutions for the membrane distillation section, other than the VMD, can be further investigated (such as the air-gap membrane distillation technology), including different methodologies to reach crystallization conditions. Moving to the power section, future works can investigate a comparative scenario with photovoltaic fields coupled with reverse osmosis plants, aiming at integrating analogous thermal processes to achieve salts crystallization that can be electrically run by the photovoltaic plant. From experimental point of view, future works can focus on the long term operational stability of the permeate for ceramic membrane for feed close to saturation.

## CRediT authorship contribution statement

**Ettore Morosini:** Writing – review & editing, Writing – original draft, Validation, Methodology, Investigation, Formal analysis, Data curation, Conceptualization. **Igor Matteo Carraretto:** Writing – review & editing, Methodology, Investigation, Conceptualization. **Giampaolo Manzolini:** Writing – review & editing, Supervision, Resources, Project administration, Investigation, Funding acquisition, Conceptualization.

## Declaration of competing interest

The authors declare that they have no known competing financial interests or personal relationships that could have appeared to influence the work reported in this paper.

## Acknowledgements

This paper is part of the DESOLINATION project that has received funding from the European Union Horizon 2020 research and innovation program under grant agreement No. 101022686.

This paper is part of the project HICLOPS “High-medium temperature closed power cycles for waste heat recovery and renewable sources” that has received funding from the MUR Progetti di Rilevante Interesse Nazionale (PRIN) Bando 2022 under grant No. 2022HMZ39A

This paper is partly carried out within the NEST - Network 4 Energy Sustainable Transition (D.D. 1243 02/08/2022, PE00000021) and received funding under the National Recovery and Resilience Plan (NRRP), Mission 4 Component 2 Investment 1.3, funded from the European Union - NextGenerationEU. This manuscript reflects only the authors’ views and opinions, neither the European Union nor the European Commission can be considered responsible for them.

## Appendix:. Preliminary economic analysis and cost estimation

The appendix summarizes the capital cost estimation of the desalination section for the preliminary economic analysis.

Results are proposed adopting the LCOW as the sole KPI of the whole desalination plant, computed as in Equation (22): this is defined as the value that brings the Net Present Value (NPV) to zero, including initial CAPEX, OPEX, the membrane replacement costs and the net cashflow from the sold freshwater produced (i.e. 3.39 $Mm^3$/year in the analysis of this work).

$$NPV = CAPEX + \sum_{i=1}^{lifetime} \frac{(OPEX + Membrane_{Replacement} - LCOW \cdot Freshwater_{yearly})}{(1+d)^i} \quad (22)$$

The capital costs assumptions are listed in Table A1: most of them are specific to the area of the HX or the membrane of each section, that is already proposed in Section 4.4. In addition to the membranes and the HXs also other components have been evaluated according to literature cost function [30] (such as the pretreatment unit, the coalescer), but their costs is found to be negligible with respect to the membranes and HX (less than 1%). Also piping and pumps are not detailed as previous techno-economic analysis found them to be almost negligible [29], considered included in the 20% of CAPEX for the indirect and contingency costs. Finally, OPEX are evaluated as fraction of the CAPEX. Additional financial assumptions are shown in Table A2, necessary for the approximate economic analysis. It is evident that since membranes are substituted every 5 years, they are actualized at the $i^{th}$ year in Equation (22), corresponding to the 5th, $10^{th}$, $15^{th}$, $20^{th}$ and $25^{th}$ year.

**Table A1**
Overview of Capital cost functions.

| Section | Cost Function | Reference |
|---|---|---|
| FO membrane | 10 €/$m^2$ | [30] |
| NF membrane | 20.4 €/$m^2$ | [30] |
| VMD membrane | 1000 €/$m^2$ | [29] |
| Heat Exchangers | 100 €/$m^2$ | [51] |

**Table A2**
Overview of financial assumptions for the economic analysis.

| Feature | Value |
|---|---|
| Plant lifetime | 30 years |
| Discount Rate ($d$) | 6% |
| OPEX | 3% of CAPEX / year |
| Substitution of membranes | Once every 5 years |
| Indirect + Contingency | 20% of CAPEX |

## Data availability

Data will be made available on request.

## References

[1] M. M. Mekonnen and A. Y. Hoekstra, "Four billion people facing severe water scarcity," *Sci. Adv.*, vol. 2, no. 2, Feb. 2016, doi: 10.1126/SCIADV.1500323.

[2] M. W. Shahzad, M. Burhan, D. Ybyraiymkul, and K. C. Ng, "Desalination Processes' Efficiency and Future Roadmap," *Entropy 2019, Vol. 21, Page 84*, vol. 21, no. 1, p. 84, Jan. 2019, doi: 10.3390/E21010084.

[3] E. Jones, M. Qadir, M. T. H. van Vliet, V. Smakhtin, and S. mu Kang, "The state of desalination and brine production: A global outlook," *Science of The Total Environment*, vol. 657, pp. 1343–1356, Mar. 2019, doi: 10.1016/J.SCITOTENV.2018.12.076.

[4] Panagopoulos A. Energetic, economic and environmental assessment of zero liquid discharge (ZLD) brackish water and seawater desalination systems. Energy Convers. Manag. May 2021;235:113957. https://doi.org/10.1016/J.ENCONMAN.2021.113957.

[5] Ghaffour N, Missimer TM, Amy GL. Technical review and evaluation of the economics of water desalination: Current and future challenges for better water supply sustainability. Desalination Jan. 2013;309:197–207. https://doi.org/10.1016/J.DESAL.2012.10.015.

[6] Subramani A, Jacangelo JG. Emerging desalination technologies for water treatment: A critical review. Water Res. May 2015;75:164–87. https://doi.org/10.1016/J.WATRES.2015.02.032.

[7] Alhaj M, Mabrouk A, Al-Ghamdi SG. Energy efficient multi-effect distillation powered by a solar linear Fresnel collector. Energy Convers. Manag. Sep. 2018;171:576–86. https://doi.org/10.1016/J.ENCONMAN.2018.05.082.

[8] Lee CH, Ho HJ, Chen WS, Iizuka A. Total Resource Circulation of Desalination Brine: A Review. Adv. Sustain. Syst. Jul. 2024;8(7):2300460. https://doi.org/10.1002/ADSU.202300460.

[9] Shalaby SM, et al. Reverse osmosis desalination systems powered by solar energy: Preheating techniques and brine disposal challenges – A detailed review. Energy Convers. Manag. Jan. 2022;251:114971. https://doi.org/10.1016/J.ENCONMAN.2021.114971.

[10] Kiefer F, Spinnler M, Sattelmayer T. Multi-Effect Vacuum Membrane Distillation systems: Model derivation and calibration. Desalination Jul. 2018;438:97–111. https://doi.org/10.1016/J.DESAL.2018.03.024.

[11] Kast W, Hohenthanner CR. Mass transfer within the gas-phase of porous media. Int. J. Heat Mass Transf. Mar. 2000;43(5):807–23. https://doi.org/10.1016/S0017-9310(99)00158-1.

[12] Poredoš P, et al. The potential of waste heat utilization in solar multistage membrane distillation: An alternative to PV + RO systems? Energy Convers. Manag. Oct. 2025;341:119977. https://doi.org/10.1016/J.ENCONMAN.2025.119977.

[13] Huang J, Zheng H, Kong H. Key pathways for efficient solar thermal desalination. Energy Convers. Manag. Jan. 2024;299:117806. https://doi.org/10.1016/J.ENCONMAN.2023.117806.

[14] Palenzuela P, Zaragoza G, Alarcón-Padilla DC, Blanco J. Evaluation of cooling technologies of concentrated solar power plants and their combination with desalination in the mediterranean area. Appl. Therm. Eng. Feb. 2013;50(2):1514–21. https://doi.org/10.1016/J.APPLTHERMALENG.2011.11.005.

[15] Palenzuela P, Ortega-Delgado B, Alarcón-Padilla DC. Comparative assessment of the annual electricity and water production by concentrating solar power and desalination plants: A case study. Appl. Therm. Eng. Aug. 2020;177:115485. https://doi.org/10.1016/J.APPLTHERMALENG.2020.115485.

[16] Aboelmaaref MM, et al. Hybrid solar desalination systems driven by parabolic trough and parabolic dish CSP technologies: Technology categorization,

thermodynamic performance and economical assessment. Energy Convers. Manag. Sep. 2020;220:113103. https://doi.org/10.1016/J.ENCONMAN.2020.113103.
[17] Olwig R, et al. Techno-economic analysis of combined concentrating solar power and desalination plant configurations in Israel and Jordan. Desalination Water Treat. 2012;41(1–3):9–25. https://doi.org/10.1080/19443994.2012.664674.
[18] Askari IB, Ameri M, Calise F. Energy, exergy and exergo-economic analysis of different water desalination technologies powered by Linear Fresnel solar field. Desalination Jan. 2018;425:37–67. https://doi.org/10.1016/J.DESAL.2017.10.008.
[19] Yuan L, Zhu Q, Zhang T, Duan R, Zhu H. Performance evaluation of a co-production system of solar thermal power generation and seawater desalination. Renew. Energy May 2021;169:1121–33. https://doi.org/10.1016/J.RENENE.2021.01.096.
[20] Sharan P, Neises T, Turchi C. Thermal desalination via supercritical CO2 Brayton cycle: Optimal system design and techno-economic analysis without reduction in cycle efficiency. Appl. Therm. Eng. Apr. 2019;152:499–514. https://doi.org/10.1016/J.APPLTHERMALENG.2019.02.039.
[21] Omar A, Saldivia D, Li Q, Barraza R, Taylor RA. Techno-economic optimization of coupling a cascaded MED system to a CSP-sCO2 power plant. Energy Convers. Manag. Nov. 2021;247:114725. https://doi.org/10.1016/J.ENCONMAN.2021.114725.
[22] Xiao T, Liu C, Liu L, Wang S, Tang J. A nuclear driven hybrid sCO2 power cycle/membrane distillation system for water-electricity cogeneration. Energy Convers. Manag. Nov. 2022;271:116329. https://doi.org/10.1016/J.ENCONMAN.2022.116329.
[23] Carraretto IM, Morosini E, Simonetti R, Astolfi M, Binotti M, Manzolini G. Thermal Desalination Through Forward Osmosis Coupled With CO2-Mixture Power Cycles for CSP Applications. SolarPACES Conference Proceedings Jul. 2023. https://doi.org/10.52825/SOLARPACES.V2I.789.
[24] Ramos-Escudero A, Vera-García F, Molina-García A, de Nicolás AP. A spatial decision framework for sustainable desalination: Mapping optimal sites for zero liquid discharge in Europe. Energy Convers. Manag. Nov. 2025;344:120226. https://doi.org/10.1016/J.ENCONMAN.2025.120226.
[25] Petrinic I, Jancic N, Jansen van Vuuren RD, Buksek H. Commercial thermo-responsive polyalkylene glycols as draw agents in forward osmosis. Desalination Aug. 2024;582:117576. https://doi.org/10.1016/J.DESAL.2024.117576.
[26] "Fraunhofer IKTS." Accessed: Oct. 23, 2025. [Online]. Available: https://www.ikts.fraunhofer.de/en.html.
[27] Colciaghi R, Simonetti R, Molinaroli L, Binotti M, Manzolini G. Potentialities of thermal responsive polymer in forward osmosis (FO) process for water desalination. Desalination Jan. 2022;519. https://doi.org/10.1016/J.DESAL.2021.115311.
[28] Al-Jariry Nadin, "Vacuum Membrane Distillation for Desalination: Experimental and Theoretical Investigations Using Inorganic Membranes," 2025. Accessed: Apr. 13, 2026. [Online]. Available: https://ltu.diva-portal.org/smash/record.jsf?pid=diva2%3A1952917&dswid=8861.
[29] Al-Jariry N, Morosini E, Lipnizki F, Carraretto IM. Analysis of high flux membranes for desalination in waste-heat driven vacuum membrane distillation plants: Experimental validation and techno-economic analysis. Desalination Feb. 2026;620:119627. https://doi.org/10.1016/J.DESAL.2025.119627.
[30] Colciaghi R, Simonetti R, Molinaroli L, Binotti M, Manzolini G. Levelized cost of water assessment for small-scale desalination plant based on forward osmosis process. Energy Convers. Manag. Nov. 2022;271:116336. https://doi.org/10.1016/J.ENCONMAN.2022.116336.
[31] "Desolination H2020 Project." [Online]. Available: https://desolination.eu/.
[32] Carraretto IM, et al. Characterization of the physical properties of the thermoresponsive block-copolymer PAGB2000 and numerical assessment of its potentialities in Forward Osmosis desalination. Polym. Test. Nov. 2023;128:108238. https://doi.org/10.1016/J.POLYMERTESTING.2023.108238.
[33] Phillip WA, Yong JS, Elimelech M. Reverse Draw Solute Permeation in Forward Osmosis: Modeling and Experiments. Environ. Sci. Technol. Jul. 2010;44(13):5170–6. https://doi.org/10.1021/ES100901N.
[34] Imbrogno A, Schäfer AI. Comparative study of nanofiltration membrane characterization devices of different dimension and configuration (cross flow and dead end). J. Memb. Sci. Sep. 2019;585:67–80. https://doi.org/10.1016/J.MEMSCI.2019.04.035.
[35] Balis E, Griffin JC, Hiibel SR. Membrane Distillation-Crystallization for inland desalination brine treatment. Sep. Purif. Technol. Jun. 2022;290:120788. https://doi.org/10.1016/J.SEPPUR.2022.120788.
[36] Doninelli M, et al. Thermal desalination from rejected heat of power cycles working with CO2-based working fluids in CSP application: A focus on the MED technology. Sustainable Energy Technologies and Assessments Dec. 2023;60:103481. https://doi.org/10.1016/J.SETA.2023.103481.
[37] Wagner MJ, Wendelin T. SolarPILOT: A power tower solar field layout and characterization tool. Solar Energy Sep. 2018;171:185–96. https://doi.org/10.1016/J.SOLENER.2018.06.063.
[38] Solar Reserve, "Crescent Dunes Solar Energy Plant." Accessed: Jan. 24, 2023. [Online]. Available: http://website.eventpower.com/paperclip/exhibitor_docs/15AE/SolarReserve_311.pdf.
[39] Gentile G, Picotti G, Binotti M, Cholette ME, Manzolini G. A comprehensive methodology for the design of solar tower external receivers. Renewable and Sustainable Energy Reviews Apr. 2024;193:114153. https://doi.org/10.1016/J.RSER.2023.114153.
[40] Span R, Wagner W. A New Equation of State for Carbon Dioxide Covering the Fluid Region from the Triple-Point Temperature to 1100 K at Pressures up to 800 MPa. J. Phys. Chem. Ref. Data Nov. 1996;25(6):1509–96. https://doi.org/10.1063/1.555991.
[41] Crespi F, Sánchez D, Rodríguez JM, Gavagnin G. A thermo-economic methodology to select sCO2 power cycles for CSP applications. Renew. Energy Mar. 2020;147:2905–12. https://doi.org/10.1016/j.renene.2018.08.023.
[42] Crespi F, Gavagnin G, Sánchez D, Martínez GS. Supercritical carbon dioxide cycles for power generation: A review. Appl. Energy Jun. 2017;195:152–83. https://doi.org/10.1016/j.apenergy.2017.02.048.
[43] Soumhi M, Zalim Y, EL Ahmadi Z, El Hamdani F, Bouzekri H. Comparative study of supercritical CO2 brayton cycles for solar towers plants in arid climates: Design and off-design performance. Energy Convers. Manag. Aug. 2025;337:119902. https://doi.org/10.1016/J.ENCONMAN.2025.119902.
[44] McCutcheon JR, Elimelech M. Influence of concentrative and dilutive internal concentration polarization on flux behavior in forward osmosis. J. Memb. Sci. Nov. 2006;284(1–2):237–47. https://doi.org/10.1016/J.MEMSCI.2006.07.049.
[45] H. Ryu, A. Mushtaq, E. Park, K. Kim, Y. K. Chang, and J. I. Han, "Dynamical Modeling of Water Flux in Forward Osmosis with Multistage Operation and Sensitivity Analysis of Model Parameters," *Water 2020, Vol. 12, Page 31*, vol. 12, no. 1, p. 31, Dec. 2019, doi: 10.3390/W12010031.
[46] Zhang J, et al. Modelling of vacuum membrane distillation. J. Memb. Sci. May 2013;434:1–9. https://doi.org/10.1016/J.MEMSCI.2013.01.048.
[47] Schnittger J, McCutcheon JR, Hoyer T, Weyd M, Voigt; I, Lerch A. Modified ceramic membranes for the treatment of highly saline mixtures utilized in vacuum membrane distillation. Desalination Dec. 2023;567:116943. https://doi.org/10.1016/J.DESAL.2023.116943.
[48] Sparrow BS. Empirical equations for the thermodynamic properties of aqueous sodium chloride. Desalination Oct. 2003;159(2):161–70. https://doi.org/10.1016/S0011-9164(03)90068-3.
[49] Carraretto IM, Morosini E, Simonetti R, Astolfi M, Binotti M, Manzolini G. "Thermal Desalination Through Forward Osmosis Coupled With CO2-Mixture Power Cycles for CSP Applications," in *SolarPACES Conference Proceedings*. TIB Open Publishing Jul. 2023. https://doi.org/10.52825/solarpaces.v2i.789.
[50] M. G. O'Connell, N. Rajendran, M. Elimelech, J. Gilron, and J. B. Dunn, "Analysis of energy, water, land and cost implications of zero and minimal liquid discharge desalination technologies," *Nature Water 2024 2:11*, vol. 2, no. 11, pp. 1116–1127, Nov. 2024, doi: 10.1038/s44221-024-00327-1.
[51] Hewitt GF, Pugh SJ. Approximate Design and Costing Methods for Heat Exchangers. Heat Transfer Engineering Feb. 2007;28(2):76–86. https://doi.org/10.1080/01457630601023229.